UPWELLING INTO THE LOWER STRATOSPHERE & TROPICAL WAVE BREAKING : EVIDENCE FROM CHEMICAL TRACERS

by

Zelalem Engida

Submitted in partial fulfillment of the requirements
for the degree of Master of Science

at

Dalhousie University
Halifax, Nova Scotia
August 2012

DALHOUSIE UNIVERSITY

DEPARTMENT OF PHYSICS AND ATMOSPHERIC SCIENCE

The undersigned hereby certify that they have read and recommend to the Faculty of Graduate Studies for acceptance a thesis entitled "UPWELLING INTO THE LOWER STRATOSPHERE & TROPICAL WAVE BREAKING : EVIDENCE FROM CHEMICAL TRACERS" by Zelalem Engida in partial fulfillment of the requirements for the degree of Master of Science.

Dated: August 16, 2012

Supervisor: _____

Readers: _____

_____

DALHOUSIE UNIVERSITY

DATE: August 16, 2012

AUTHOR: Zelalem Engida

TITLE: UPWELLING INTO THE LOWER STRATOSPHERE & TROPICAL WAVE BREAKING : EVIDENCE FROM CHEMICAL TRACERS

DEPARTMENT OR SCHOOL: Department of Physics and Atmospheric Science

DEGREE: M.Sc. CONVOCATION: October YEAR: 2012

Signature of Author

To

my mother, Etaba

and

the late Abaye, my mother in-law

TABLE OF CONTENTS

LIST OF FIGURES

ABSTRACT

We use 2005 - 2010 measurements from the Microwave Limb Sounder (MLS) instrument to calculate the deseasonalized anomalies of tropical mean water vapor (H_2O), carbon monoxide (CO), and nitrous oxide (N_2O) on the 68 hPa surface. We then calculate the spatial maps of the coherence between the tropical mean tracer measurements and reanalysis temperature on the 100 hPa surface, in both the subseasonal and multiyear time windows. In the multiyear time window, the spatial pattern of the coherence, and the time lags, indicate that fluctuations in 100 hPa temperature affect 68 hPa H_2O through changes in dehydration efficiency. In the subseasonal time window, the coherence between 100 hPa temperature and 68 hPa H_2O is mediated through changes in upwelling driven by the dissipation of tropical Rossby waves. On subseasonal timescales, the 68 hPa anomalies in tropical mean CO are strongly coherent with the Madden Julian Oscillation (MJO).

LIST OF ABBREVIATIONS AND SYMBOLS USED

Abbreviation	Description
ACE-FTS	Atmospheric Chemistry Experiment-Fourier Transform Spectrometer
BDC	Brewer-Dobson Circulation
BLN	Boehm-Lee-Norton
COSMIC	Constellation Observing System for Meteorology, Ionosphere, and Climate
CPT	Cold Point Tropopause
CSA	Canadian Space Agency
ECMWF	European Center For Medium Weather Forecast
ENSO	El Niño-Southern Oscillation
EOF	Emperical Orthogonal Function
EOFd	EOF of daily mean data
EOFm	EOF of monthly mean data
EP	Eliassen-Palm flux
ERRA	ECMWF Re-analysis
GCM	Global Climate Model
GEOS	Goddard Earth Observing System
GES-DISC	Goddard Earth Sciences Data and Information Services Center
GPS	Global Positioning System
hPa	hecto Pascal
MERRA	Modern Era Retrospective Analysis for Research and Application
MJO	Madden Julian Oscillation
MLS	Microwave Limb Sounding
MSU	Microwave Sensing Units
NASA	National Aeronautics and Space Administration

Abbreviation	Description
NCAR	National Center for Atmospheric Research
NCEP	National Centers for Environmental Prediction
NOAA	National Oceanic and Atmospheric Administration
NSERC	Natural Science and Engineering Research Council of Canada
ODS	Ozone Depleting Substance
OLR	Outgoing Longwave Radiation
PC	Principal Component
PCA	Principal Component Analysis
PCd	Principal Component of daily mean data
PCdm	monthly mean of PCd
PCm	Principal Component of monthly mean data
ppbv	parts per billion
ppmv	parts per million
ppv	parts per volume
PVU	Potential Vorticity Unit
QBO	Quasi-Biennial Oscillation
RMM1	Real-time Multivariate MJO index 1
SCISAT	Science Satellite
SMR	Saturation Mixing Ratio
SO	Southern Oscillation
SOI	Southern Oscillation Indiex
SST	Sea Surface Temperature
STE	Stratosphere Troposphere Exchange
STE	Stratosphere-Troposphere-Exchange
TIO	Tropical Intraseasonal Oscillation
TTL	Tropical Tropopause Layer
UARS	Upper Atmosphere Research Satellite
WMO	World Meteorological Organization

Symbol	Description	Units
$\bar{\kappa}$	mean coherence	
$\bar{\tau}$	mean time lag	days
$\gamma_{x,x}$	auto-covariance of any variable x	unit of x^2
$\Gamma_{x,x}$	auto-covariance of any variable x	unit of x^2
$\gamma_{x,y}$	cross-covariance of any variables x and y	unit of x^2 or y^2
$\Gamma_{x,y}$	cross-covariance of any variables x and y	unit of x^2 or y^2
$\kappa^2_{x,y}$	coherence squared of x and y	
$\kappa^2_{x,y}$	coherence squared of x and y	
ω	frequency	cycle day^{-1}
$\Phi_{x,y}$	phase difference between x and y	radian
σ^2_p	predicted variance	unit of x^2
σ^2_x	total variance of variable x	unit of x^2
τ	time lag	days
S	variance-covariance matrix	
$\mathbf{S}^d$	diagonalized matrix **S**	
X'	a matrix of anomaly data	
$A_{x,y}$	amplitude spectrum	unit of x or y
CH_4	Methane	
CO	carbon monoxide	
H_2O	water vapor	
N_2O	nitrous oxide	
NO	nitric oxide	
NO_2	nitrogen dioxide	
NO_x	family name for NO and NO_2	
$O(^1D)$	excited oxygen atom	
OH	hydroxyl radical	
OH_x	family name for hydroxyl radicals	
U50	50 hPa zonal wind anomaly	m s^{-1}

ACKNOWLEDGEMENTS

Thanks to God, I am finally here to acknowledge those who helped make this thesis a reality.

First of all, I sincerely thank Ian Folkins for believing in my ability to take on this study and for his guidance throughout my time at Dalhousie. His kindness, encouragement and extraordinary patience helped me stay focused. Glen Lesins, my committee member, also deserves my appreciation for his valuable comments during writing this thesis. Thanks to Eric Oliver for his comments which resulted in a major change to this thesis.

I also would like to thank Dalhousie University, the Canadian Space Agency (CSA) and the Natural Science and Engineering Research Council of Canada (NSERC) for the full and partial financial supports. Without their generous funding, finishing my study was unthinkable.

Thanks to Samuel Lazerson of Princeton Plasma Physics Lab. for his help in programming with MATLAB at the earliest stage of my research. All the data used in this thesis were obtained free of charge. Thanks also to Toni Mitovski for our limited time discussing data formats.

I have several people to thank but I am afraid I can name them all. All the good people I have come across at Dalhousie, and elsewhere in Halifax, please take your thanks.

A special thanks to my mother whose prayers, from thousands of miles away, have given me the strength. I know you are hoping to see me do more than this in academics, but I am sure this tells you I am moving on.

To my wife, thanks for listening patiently to my endless, sometimes completely nonsense to you, science talks and for taking care of our little son.

CHAPTER 1

INTRODUCTION

1.1 Motivation

The chemical composition of the stratosphere is strongly affected by the composition of the air upwelling across the tropopause into the stratosphere. Until recently, it was believed that this upward flow was driven by the breaking and momentum transfer of waves in the extratropics (*Holton et al.*, 1995). However, there is increasing evidence, from both diagnostic interpretations of reanalysis data (*Kerr-Munslow and Norton*, 2006; *Randel et al.*, 2008) and model simulations (*Boehm and Lee*, 2003; *Norton*, 2006; *Garny et al.*, 2011b) that much of the upwelling in the lower tropical stratosphere is forced by the dissipation of tropical waves. This upwelling source has been called the Boehm-Lee-Norton (BLN) mechanism (*Ryu and Lee*, 2010). We provide additional support for this mechanism by demonstrating that much of the tracer variability in tropical lower stratosphere is coherent with tropical Rossby wave activity.

On multiyear timescales, tracer variability in the lower stratosphere is dominated by upwelling variability associated with the El Niño-Southern Oscillation (ENSO) (*Garcia and Randel*, 2008; *Randel et al.*, 2009; *Calvo et al.*, 2010) and the Quasi Biennial Oscillation (QBO) (*Randel et al.*, 2004; *Fueglistaler and Haynes*, 2005; *Schoeberl et al.*, 2008b). It is therefore most appropriate to look for tracer variability from the BLN mechanism on subseasonal timescales (30 - 90 days). The main source of variance in convective activity in this time window is the Madden Julian Oscillation (MJO). During MJO events, a large envelope of enhanced convection propagates eastward across the

Indian Ocean toward the Western Pacific at a speed of $\sim$5 - 8 m s^{-1} (*Zhang*, 2005; *Monier et al.*, 2010). MJO events modulate the generation of Rossby waves, and should therefore generate fluctuations in the mixing ratios of chemical tracers in the lower stratosphere through the BLN mechanism.

Rossby waves generate wind and pressure anomalies which have characteristic horizontal patterns near the tropical tropopause (*Ryu and Lee*, 2010). We compare these patterns with maps of the coherence between temperature anomalies on the 100 hPa surface and anomalies in tropical mean lower stratospheric tracer mixing ratios. We interpret similarities between the two maps, in the subseasonal time window, as evidence that tracer variability in the lower stratosphere is forced by Rossby waves. We also calculate maps of the coherence between 100 hPa temperature fluctuations and tropical mean lower stratospheric tracer anomalies in the multiyear time window. These maps are compared with the pattern of temperature fluctuations on the 100 hPa surface associated with ENSO and the QBO.

1.2 Thesis Organization

Chapter 1 is a literature review. Descriptions of data used in this thesis are presented in chapter 2. We also do a simple data comparison and prepare the data for further analysis. Chapter 3 contains data analysis. Chapter 4 presents the main results. Chapter 5 discusses the conclusions of the research.

1.3 Literature Review

The accuracy of Global Climate Models (GCMs) partly depends on how well the dynamical, chemical and radiative coupling between the stratosphere and troposphere are represented (*Holton et al.*, 1995). Such couplings between these two layers of the atmosphere are achieved through a process called Stratosphere-Troposphere-Exchange (STE). STE takes place when air parcels cross the boundary, called tropopause, between the troposphere and stratosphere. According to World Meteorological Organization (WMO), the tropopause is defined as the lowest level at which the lapse rate decreases to 2 C/km or less, provided

that the average lapse rate between this level and all higher levels within 2 km does not exceed 2 C/km. This is specifically called the Lapse Rate Tropopause (LRT), or simply thermal tropopause (TP) (*Gettelman et al.*, 2001). However, different authors have used different working definitions of the tropopause. The level of minimum Saturation Mixing Ratio (SMR) of water vapor with respect to ice is sometimes considered the tropopause level (*Zhou et al.*, 2001). The minimum temperature level in the vertical temperature profile is defined as Cold Point Tropopause (CPT) (eg., *Selkirk*, 1993; *Gettelman et al.*, 2001). The dynamical tropopause (of extratropics) is defined as an isosurface of 2 PVU (1 PVU=$10^6 K kg m^2 s^{-1}$) (*Martius et al.*, 2008). In most cases, however, such a level is usually not considered as a material boundary.

Even though there are distinctions between the stratosphere and troposphere with regard to time scales of vertical advection and the resulting distinctions in profiles of chemical species, the two layers are strongly linked. As a result, especially in the tropics, there is a shallow layer that exhibits both stratospheric and tropospheric characteristics. Such a layer has been called the Tropical Tropopause Layer (TTL) (*Selkirk*,1993; *Folkins et al.*,1999; *Gettelman and de F. Forster*, 2002). Under clear sky conditions the time averaged vertical motion in the TTL is upward as the heating rate becomes positive above about 15 km (base of TTL) (*Folkins et al.*, 1999). Thus, air entering the TTL will likely enter into the stratosphere and eventually sinks in the extratropics after vertical and meridional transport by the Brewer-Dobson Circulation (BDC).

There are chemical species whose upward transport alters stratospheric chemistry such as ozone depletion rates and affects stratospheric climate through changes in radiative balance. It has been noted in some model simulations that an increase in STE due to anthropogenic climate change (*Garcia and Randel*, 2008) could lead to an earlier polar stratospheric ozone recovery dates (*Waugh et al.*, 2009). On the other hand, downward transport of ozone itself has been reported to be a major air pollution problem at higher latitudes (eg., *Hegglin and Shepherd*, 2009) . Upward transport of anthropogenic chemical species has a significant role in the budget of long lived chemicals such as CH_4, CO and N_2O in the troposphere. This means that STE could lead to tropospheric response to stratospheric changes and vice versa.

Convective overshooting by which air gets transported directly into the stratosphere has been suggested as one pathway for STE (*Dessler*, 2002). However, the occurrence rate of such intense clouds is too small to reconcile the observed variability in stratospheric mixing ratios (*Folkins et al.*, 1999; *Gettelman et al.*, 2002). In the case of water vapor, the effect of convective overshooting is more complex. Dry air injected into the lower stratosphere could contribute to the dryness there (*Newell and Gould-Stewart*, 1981). But, if sufficient ice crystals are transported within the overshoot, their eventual evaporation could lead to stratospheric moistening. Currently, the widely accepted hypothesis for transport in the TTL is slow large scale ascent called upwelling. This mechanism is driven by wave forcing both in the tropics and extratropics (*Garny et al.*, 2011b).

Thermal wind balance requires westerly stratospheric winds in the extratropics during the long cold polar nights. Such conditions lead to an increased wind shear in the background environment. Planetary-scale Rossby waves of tropospheric origin can then propagate upward with little damping from the background. As the waves continue to propagate upward they continue to grow in amplitude to the point of breaking. Upward transport of negative angular momentum by dissipating planetary scale Rossby waves (*Holton and Lindzen*, 1972; *Dunkerton*, 1985) drives the poleward circulation in the stratosphere, a phenomenon called "Wave drag" (*Holton et al.*, 1995). By mass continuity, this poleward transport induces upwelling in the tropics. In the extratropical stratosphere, radiative cooling causes downwelling and completes the Brewer-Dobson Circulation. During the summer, thermal winds in the lower stratosphere become easterly and vertical propagation of Rossby waves is restricted. As a result, the BDC weakens due to insufficient wave drag. Planetary scale Rossby waves generation in the troposphere is dependent on land-ocean contrast, which is highest in the Northern Hemisphere (NH). Therefore, the BDC is stronger in the NH than in the Southern Hemisphere (SH).

Tropical waves in the lower stratosphere dissipate by thermal damping which is directly proportional to frequency of the waves (*Garcia and Salby*, 1987). When the zonal mean wind in the background atmosphere is easterly, the effective (Doppler) frequency of westward propagating quasi-stationary waves decreases. The decrease in frequency causes increased thermal wave damping (*Garny et al.*, 2011b). In an easterly shear background

there is an increase in wave damping with height of westward propagating waves. Thus, the environment will prevent further upward propagation of the waves. Although the direct effect of deep convection on upward transport in the TTL is small , latent heat release in tropical deep convection has a major role in the generation of tropical waves (*Gill*, 1980) that drive upwelling in the TTL.

In the lower stratosphere, the chemical lifetimes of some chemicals are longer than transport times. This means that variability in mixing ratios will be mainly driven by transport. Therefore, it is possible to study transport in the TTL and its response to dynamics of different timescales using conserved chemical tracers.

The main focus of this thesis is the upward transport of chemical tracers (namely, water vapor, carbon monoxide and nitrous oxide, with special attention to water vapor) across the TTL. The three chemical species used here are chosen as chemical tracers due to their long lifetime against oxidation in the tropical lower stratosphere. Water vapor is a condensible tracer while the other two are dry/non-condensible tracers. The statistical relationships among deseasonalized tracer anomalies at 68 hPa level ($\sim$18.8km) with near tropical tropopause level, 100 hPa ($\sim$16.6 km), temperatures will be explored in different time windows. The results will be attributed to specific dynamical modes of variability. Since the annual and semiannual cyles will be removed from the datasets the remaining dominant modes to look for are multiyear (QBO and ENSO) and subseasonal (MJO).

1.3.1 Dynamical Modes of Interest

The tropical atmosphere shows different modes of variability with time scales ranging from hours to several years. Some are organized and have well defined return periods (eg., annual and seasonal cycles) and some are pulse like in nature with return periods that are not well defined (eg., MJO and ENSO). Other modes of variability show nearly well defined range of periods (eg., QBO). Each of these modes of variability express themselves in atmospheric fields that they impact. For example, there are annual and seasonal cycles in almost all atmospheric variables including air temperature, rainfall, wind, cloud cover, relative humidity and several others. The discussion of dynamical modes here will be limited to only those that are identifiable in deseasonalized anomalies. These are the MJO,

QBO and ENSO.

1.3.2 The Madden Julian Oscillation

The Madden Julian Oscillation (*Madden and Julian*, 1971, 1972) is a planetary scale oscillation in the tropical troposphere where a complex, organized, multiscaled convection feature propagates in the West-East direction. The MJO was first reported by Roland A. Madden and Paul R. Julian in their 1971 work published at Journal Of Atmospheric Science. In this work they accidentally realized the existence of peaks in the co-spectrum of 850 and 150 hPa zonal wind components in the period range 41-53 days.

> "In the course of an investigation of tropical wind data designed to provide analyses over a broader frequency range and to study the non-stationary aspects of the aforementioned wave modes, we stumbled up on an apparent long-period oscillation in the station pressure and zonal wind componenets at Canton Island (3^o S, 172^o W)." *Madden and Julian*, 1971.

In the same 41-53 days period window of oscillation, they also found spectral peaks in zonal wind components of lower and upper troposphere with no peaks in the 700-400 hPa layer. Furthering their analyses to compute the cross spectra between the station pressures and wind components they showed station pressure oscillations were in phase with zonal wind components in the lower troposphere and out of phase with upper troposphere zonal wind components.

The spatial extent of the MJO was first estimated from coherence squared and phase analyses of 24 station pressure and zonal wind records relative to Canton Island (3^o S, 172^o W) (*Madden and Julian*, 1972). The authors speculated that the eastern equatorial Indian Ocean was the source of the disturbances that propagated eastward as far as the west coasts of central America. They also found meridional propagation of the MJO was weaker and that the MJO to be confined to the 10^oN-10^oS latitude range.

The phase and strength of the MJO are described by multivariate indices (*Wheeler and Hendon*, 2004). The life cycle (i.e., the phase and strength) of a single MJO event can be traced using these indices. There are eight phases of MJO depending on the location

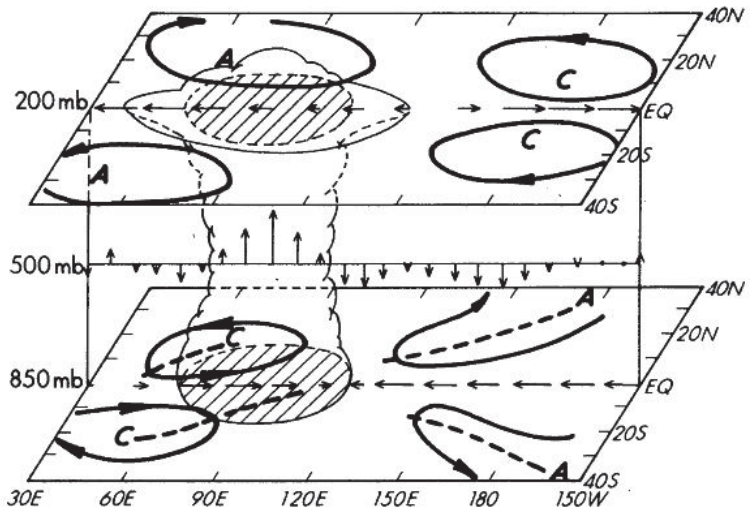

Figure 1.1: Schematic diagram of the large-scale wind structure associated with the MJO in central Indian Ocean (phase-3). The cloud symbol indicates the convective center. Shaded regions correspond to areas of low OLR anomalies. Zonal wind anomalies at 850 and 200 hPa are indicated by horizontal arrows. Vertical motions at 500 hPa are shown by arrows in longitude-height plane. Bold letters "A" and "C" mark the anticyclonic and cyclonic circulation centers, respectively. Dashed lines mark troughs and ridges. Taken from *Rui and Wang* (1990) .

of convection centres. Figure 1.1 shows major features in phase 3 of MJO where the convection center is over Indian ocean. Nearby locations of the convection centre are characterized by low level (850 hPa) convergence as shown by the two cyclonic centres. At upper levels (200 hPa), these centres become anticyclonic. There is also a reversal of the zonal winds as shown by the horizontal arrows. To the east of the convection center there are centres of upper level convergence and low level divergence with a net effect of subsidence warming. Also, the clear sky condition associated with this warming allows more solar radiation that eventually causes warm sea surface temperatures (SST). Warm SST generates moisture convergence that once again triggers convection.

The MJO is now considered as the dominant component of sub-seasonal variability in the tropics with periods spanning 30-90 days (*Zhang*, 2005; *Monier et al.*, 2010). The MJO in the troposphere is mainly characterized as organized equatorially trapped planetary scale convective disturbances that slowly propagate eastward at a mean phase speed of $\sim$ 5-8 ms^{-1} (*Zhang*, 2005; *Majda and Stechmann*, 2011). Figure 1.2 is constructed using

Lanczos 30-90 day band pass filtering (*Duchon*, 1979) of deseasonalized anomalies of daily mean outgoing long wave radiation (OLR) and rainfall data for the year 2008. The left hand panel in Figure 1.2 shows the eastward propagation in OLR with low OLR (blue) regions moving eastward between roughly 60^{o}E and 180^{o}E. This is a proxy for the eastward migration of tropical convection as low OLR areas are associated with cloudy conditions. The right panel in this figure confirms this as the positive rainfall anomalies move in the same direction as the OLR anomalies and there is a coincidence in the regimes of the two anomalies. The MJO phase speeds are different from event to event. Thus, there have been faster and slower MJO events in the same year as shown in the right panel.

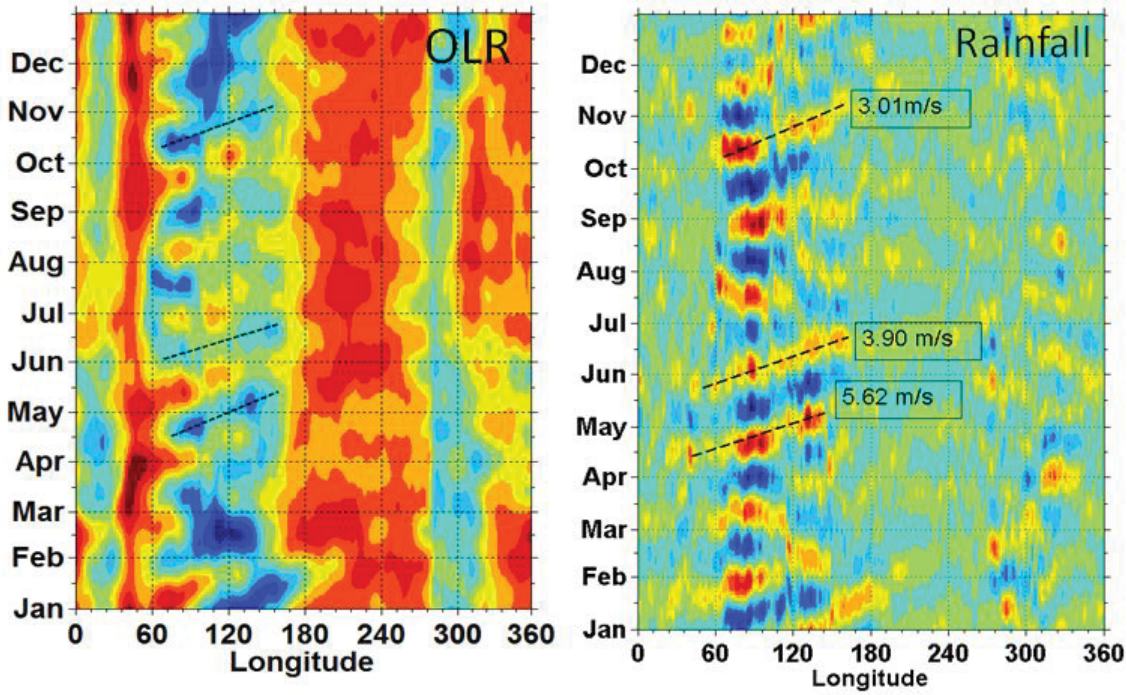

Figure 1.2: MJO signals in deseasonalized anomalies of OLR (W/m^2) from NOAA (left) and TRMM daily mean rain fall (mm/day) (right). Both data are for Jan-Dec 2008 averaged between 10^{o}N and 10^{o}S , and are 30-90 days bandpass filtered using Lanczos filter. Dashed lines show selected MJO events with values in boxes in the right panel showing phase speeds of MJO.

The relocation of convective centres by the MJO is expected to affect tropical tropopause temperatures by relocating the heating associated with latent heat release. As a heating source in the troposphere, MJO can cause the generation of atmospheric waves in mid and

upper troposphere (*Ryu et al.*, 2008). The waves affect temperatures and mixing ratios in the tropical stratosphere in a fashion that does not necessarily show MJO like features.

1.3.2.1 MJO Heating and Wave Generation

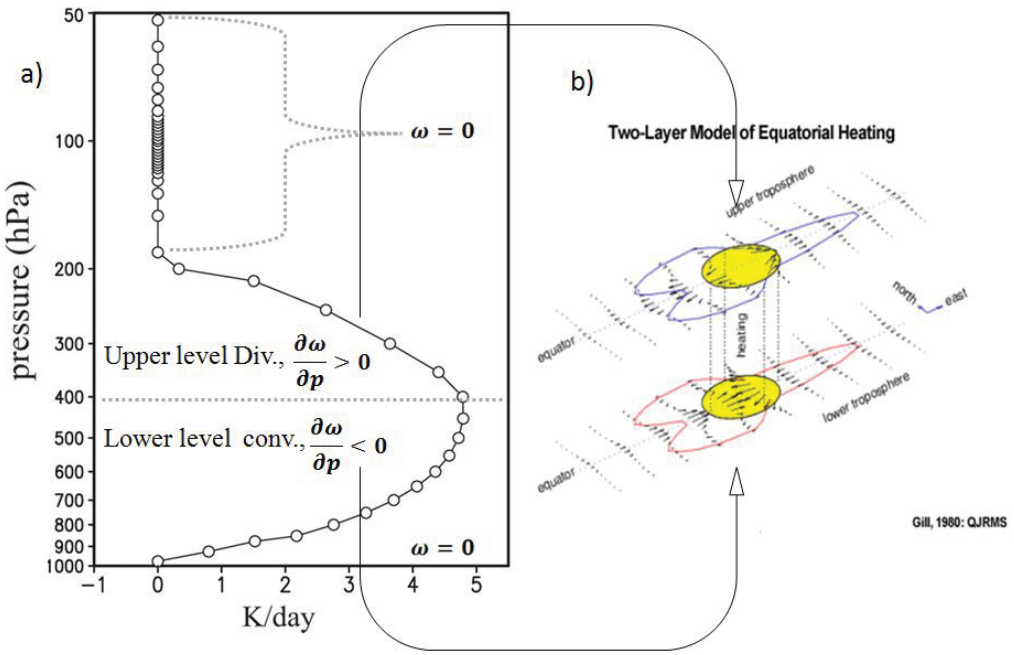

Figure 1.3: a) Modelled vertical profile of idealized convective heating at 150^oE and the equator. Circles indicate model grid levels (Adapted from *Ryu et al.* (2008)) and b) Two layer model results of simplified heating at the equator resulting in surface low, high aloft, and geostrophic wind response. Arrows indicate wind vectors. The cylinder like region with yellow shaded top and base represents the center of heating. And, blue and red contours show streamfunctions. (Taken and slightly adapted in the caption from https://www.meted.ucar.edu/search/details.php?id=2018).

The importance of convective heating to the generation of tropical waves has been touched earlier in this chapter. In the following discussion, the importance of MJO heating will be discussed using an idealized model (*Gill*, 1980). In the tropics, horizontal temperature gradients are weaker than in mid latitudes. As a result, horizontal advection will not be strong enough to balance the strong heating in the vicinity of moist convections. So, the only balance is achieved through vertical motion. A typical convective event in the tropics could induce latent heating as as high as 5 K/day near 400 hPa (*Ryu et al.*, 2008). Figure 1.3a shows an idealized convective heating profile at a single location

(150^oE, Equator). It can be assumed that the vertical speed, ω, is zero both at the surface and just above the height level where the heating is none zero. Due to weak horizontal temperature advection, the heating at lower levels induces upward motion and the upward speed increases with height as the long as the heating does the same. At levels above the maximum heating ($\sim$ 400 hPa in this case) the upward speed decreases with height and becomes zero at the level where the heating itself is zero. This means that the ascent triggered by the heating does not reach the tropopause which is at about 100 hPa and there seem to be no effect of the heating on this level. However, the ascent in the lower levels generates negative pressure perturbations such that the horizontal wind converges towards the heating center as shown in the lower yellow circular region in Figure 1.3b. At the upper level of Figure 1.3b, two Rossby waves (each on either side of the equator) are generated to the west of the heating center. On the same level, equatorial Kelvin waves are generated to the east of the heating. This is, in fact, what is called Gill response to heating, a simplified response of the atmosphere to heating (*Gill*, 1980). The Gill model assumes a symmetric heating located at the equator and a resting background. However, the none zero zonal wind in the background interacts with the waves. The heating source also moves with an MJO speed (*Hendon and Salby*, 1994; *Majda and Stechmann*, 2011). Despite its limitations, the Gill model will be accepted in this thesis as it is found sufficient enough to create a dynamical framework to understand the main results.

1.3.2.2 Wave Forcing and Upper Level Meridional Circulations

The two types of overturning meridional circulations are shown by solid arrows in the schematic Figure 1.4 (*Garny et al.*, 2011b). Dashed arrows of different thickness represent wave propagation directions. The light gray areas represent regions of Eliassen-Palm flux (EP-flux) convergence. The EP-flux convergence region of the winter hemisphere high latitude is placed far from the tropopause, which is shown by a thin dashed line nearly parallel to the latitude axis. This is to indicate the longer vertical distance the waves penetrate into the stratosphere before dissipation during the winter. In the summer hemisphere, EP-flux convergence region is closer to the tropopuse and implies less wave breaking in the stratosphere. In the winter hemisphere, the traditional hemispheric-wide Brewer-Dobson

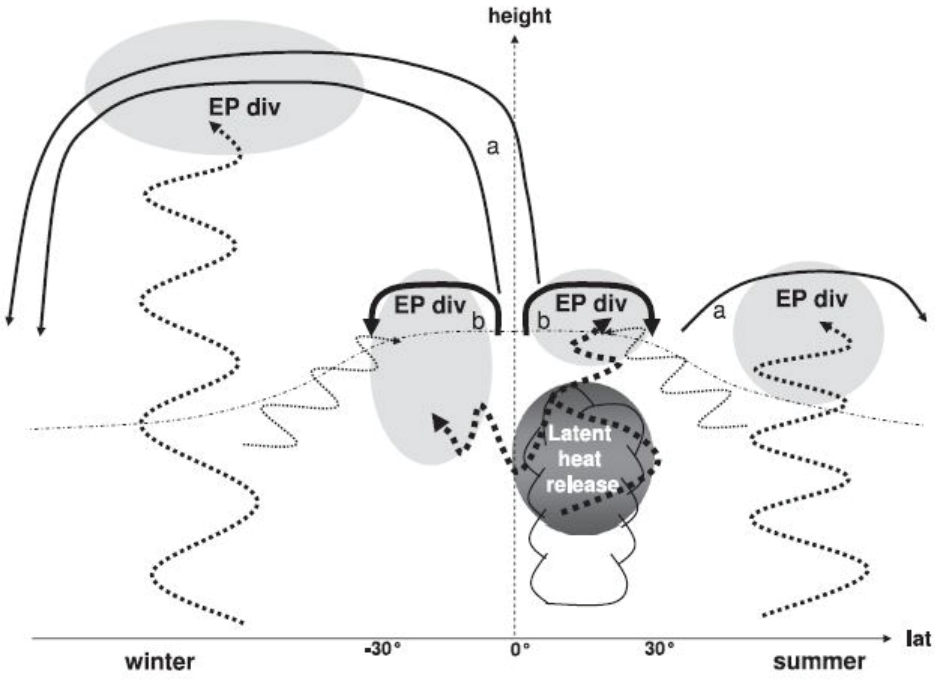

Figure 1.4: Idealized schematic of the two branches of the meridional circulation in the stratosphere and its wave driving. Wave flux convergence is indicated as light gray patches (negative EP flux divergence). The global classical BDC (arrow a) is driven by extratropical waves and a deep hemisphere-wide cell exists in the winter hemisphere. The secondary circulation (arrow b) is confined to the (sub)tropical lower stratosphere and driven locally by wave dissipation. Both tropical waves, which are mostly generated by strong deep convection in the summer tropics, and extratropical waves, which are refracted to low latitudes, contribute to the wave flux convergence in the upper troposphere/lower stratosphere. Taken from *Garny et al.* (2011b).

Circulation is at its maximum strength. As mentioned earlier, this circulation is driven by the extra-tropical wave pumping (*Holton et al.*, 1995).

The darker region on the upper part of a cloud symbol represents a latent heat release region that is consistent with the region of bulging heating curve in Figure 1.3a. This heating generates tropical waves that also propagate upward as indicated by the bold dashed arrows. These waves dissipate in the lower subtropical stratosphere as shown by the two inner (EP-flux) convergence regions to drive a secondary smaller meridional circulation that enhances tropical upwelling by BDC. There are also contributions to the tropical wave forcing from refracting extratropical shorter (synoptic-scale) waves that

dissipate in the subtropics. Given that the mean zonal winds are easterly in the subtropical lower stratosphere, the waves that are dissipated in this region need to be low frequency waves with a westward phase speed. Such waves include the Rossby waves shown in the upper troposphere in Figure 1.3b. Therefore, MJO heating generates tropical waves and the waves in turn enhance tropical upwelling.

1.3.3 The Quasi Biennial Oscillation

The QBO is the dominant dynamical mode of variability in the tropical stratosphere (*Baldwin et al.*, 2001). This oscillation is mainly observed in the alternating and downward propagating zonal wind regimes of average period of 28 months (*Baldwin et al.*, 2001). The QBO is said to be in westerly phase when the zonal mean wind at 44 hPa exceeds +5 m s^{-1} and in easterly phase when the zonal mean wind is less than -5 m s^{-1} (*Pascoe et al.*, 2005). The QBO was discovered by R. J. Reed (1961) and A. Ebdon (1960) who worked independently on balloon data from Canton Island "3^o S, 172^o W". Figure 1.5 shows both the periodic phase reversal and downward propagation ($\sim$1 km/month) of zonal winds.

A wide spectrum of tropical gravity waves are believed to initiate the QBO (*Baldwin et al.*, 2001). The QBO affects tropopause temperatures and chemical tracer transport across the tropopause (*Dunkerton*, 2001; *Schoeberl et al.*, 2008b). In the tropical lower stratosphere a thermal wind balance can be invoked to explain the temperature response (*Haynes*, 2005) of the tropical tropopause to downward propagating QBO wind regimes (*Pascoe et al.*, 2005). Accordingly, when the westerly phase of QBO comes closer to the equatorial tropopause the westerly geostrophic wind shear becomes stronger. This will intensify the warm temperatures (*Dunkerton*, 1985) in the warm pool area and warm up areas out side the warm pool along the equator through thermal wind balance. The reverse happens during the easterly phase of QBO. The QBO signal in the tropical tropopause temperatures is confined to the tropics and it is zonally symmetric (*Randel et al.*, 2000; *Zhou et al.*, 2001; *Zhou et al.*, 2004). From the slopes of individual wind regimes in Figure 1.5 it is apparent that the westerlies descend faster than the easterlies (*Naujokat*, 1986). The intensity of the colors suggest the easterly regimes are stronger.

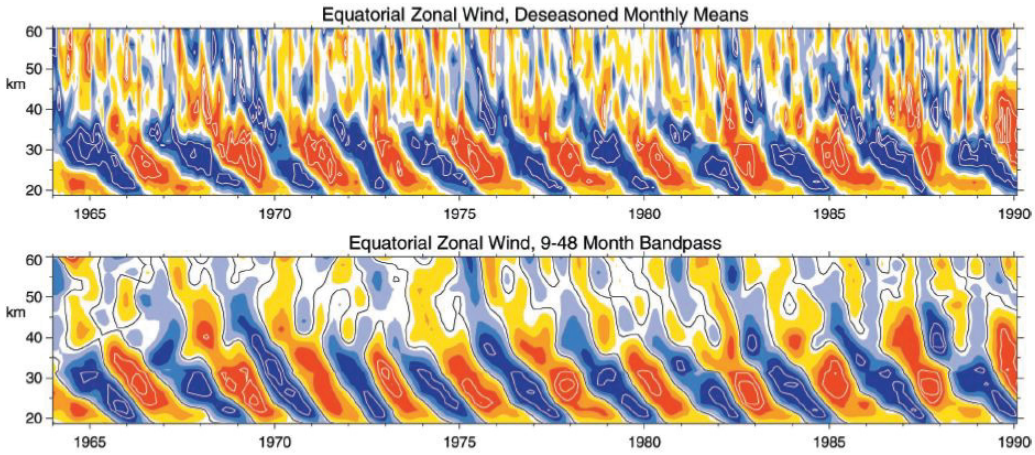

Figure 1.5: (top) Time-height section of the monthly-mean zonal wind component (m s^{-1}), with the seasonal cycle removed, for 1964-1990. Below 31 km, equatorial radiosonde data are used from Canton Island (2.88^o N, January 1964 to August 1967), Gan/Maldive Islands (0.78^o S, September 1967 to December 1975), and Singapore (1.48^o N, January 1976 to February 1990). Above 31 km, rocketsonde data from Kwajalein (8.78^o N) and Ascension Island (8.08^o S) are shown. The contour interval is 6 m s^{-1}, with the band between 23 and 13 unshaded. Red represents positive (westerly) winds. After Gray et al. [2001]. In the bottom panel the data are band-pass filtered to retain periods between 9 and 48 months. Figure taken from (*Baldwin et al.*, 2001)

1.3.4 ENSO

ENSO defines a dominant tropical interannual variability in the atmosphere-ocean coupled system. The word itself comes from two words namely El Niño (oceanic component) and Southern Oscillation (atmospheric component). The existence of this atmosphere-ocean coupled system depends on a positive feedback process (*Bjerknes*, 1969). The equatorial low level (trade) winds in the tropical Hadley circulation blow from east to west. Sea level gradients of about 40 cm build in the east-west Pacific in response to the surface wind stress (*Neelin et al.*, 1998). During the Northern Hemisphere winter-spring time, the southern equatorial ocean surfaces become warmer. The sea level gradients cause ocean surface currents that push the warmer surface water from east to west and cause upwelling of colder deep water on the eastern side of the Pacific (*Neelin et al.*, 1998). Figure 1.6a shows the resulting sea surface temperature (SST) contrasts with the blue and red/orange colors representing colder and warmer SST conditions. Convection develops over the region where the SST is warm enough to evaporate sufficient sea water. At upper

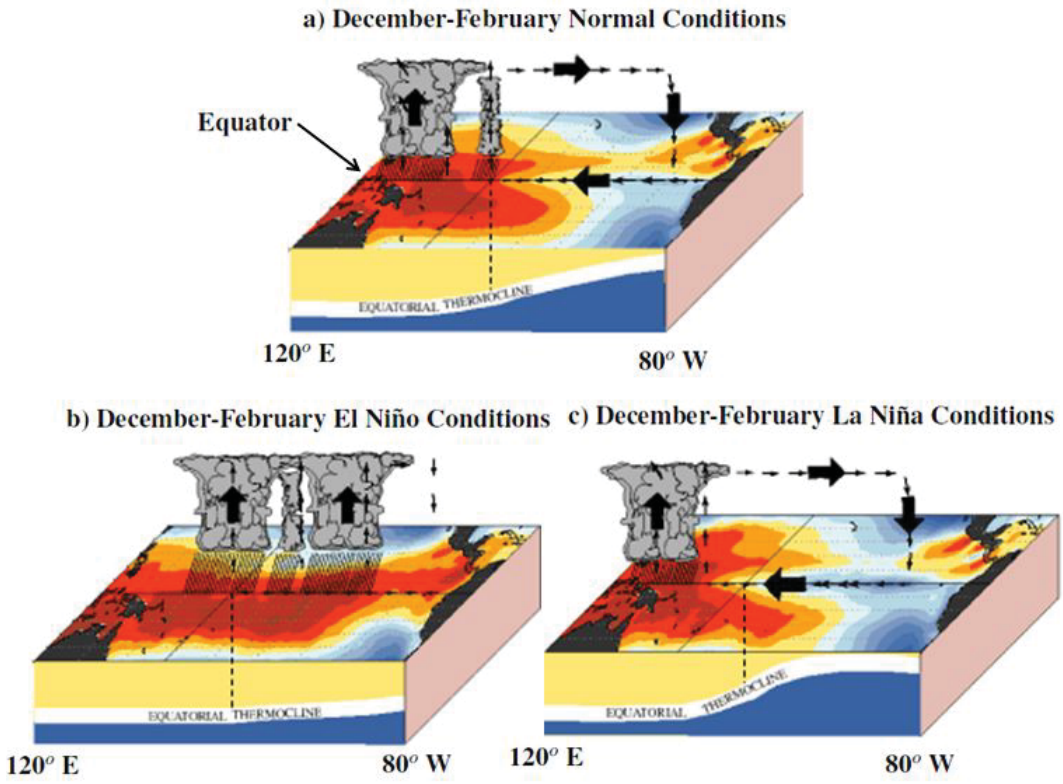

Figure 1.6: Schematic view of sea surface temperature and tropical rainfall in the the equatorial Pacific Ocean during normal, El Niño, and La Niña conditions. The sea-surface temperature is shaded: blue-cold and orange-warm. The dark arrows indicate the direction of air movement in the atmosphere: upward arrows are associated with clouds and rainfall and downward-pointing arrows are associated with a general lack of rainfall. This Figure is taken from the International Research Institute for Climate Science(http://iri.columbia.edu/climate/ENSO/background/basics.html)

levels, there will be a westerly flow from the top of the convective systems to counter balance the surface easterly flow. The subsidence over the eastern Pacific closes what is now called the Walker circulation (shown by the arrows in Figure 1.6a). This seemingly at equilibrium condition, however, has a natural oscillation in which the Walker circulation becomes weaker or stronger than normal in response to a see-saw like oscillation in sea level pressures between the west and east Pacific. In 1920's Sir Gilbert Walker noticed the out of phase sea level pressure variations between Darwin (western Pacific), and Tahiti (eastern Pacific) Islands and called it the Southern Oscillation (SO), both islands being in the south. The sea level pressure difference between Darwin and Tahiti is called Southern

Oscillation Index (SOI), one of the diagnostics to gauge the phase and strength of ENSO. The two extreme phases of ENSO are called El Niño and La Niña.

In some years, anomalously warm water appears near the coast of Ecuador and Peru during December-February causing an eastward shift of convection and weakening of the trade winds. This condition is called El Niño and shown in Figure 1.6b. During the opposite phase of El Niño, called La Niña, the central and eastern equatorial Pacific SST gets colder than normal during the same December-February period. This condition simply intensifies the Walker circulation as shown in Figure 1.6c. The approximate return period of El Niño or La Niña is about 2-7 years (*Jiang et al.*,1995; *Neelin et al.*,1998; *MacMynowski and Tziperman*, 2008). The time period between onset and cessation of individual phases is approximately 12 to 18 months with La Niña's tending to last longer (*Okumura and Deser*, 2010). It is often observed that El Niño or La Niña come one after the other. For example, the strongest on record El Niño of the 1997-98 was followed by one of the longest La Niña's on record that lasted from mid-1998 to early 2001 (Source: http://www.cpc.ncep.noaa.gov/products/analysis-monitoring/ensostuff/ensoyears.shtml). In recent years, El Niño and La Niña have occurred during 2007-2008 and 2009-2010 respectively. ENSO impacts the global climate variability (*McLean et al.*, 2009) through its interaction with the meridional Hadley circulation, a phenomenon called global teleconnection (*Bjerknes*, 1969). *McLean et al.* (2009) found 72% of the variability in satellite microwave sensing units (MSU) global tropospheric temperature anomalies from which volcanic effects were removed and 81% of the same anomalies in the tropics accounted for by changes in SOI. ENSO has also been shown to have different signatures on surface to lower stratospheric temperatures on a global scale (eg. *Trenberth and Smith*, 2006).

1.3.4.1 ENSO Signatures on Cold Point Tropopause (CPT) Temperature

The relocation of convective systems during the ENSO cycle can be expected to be associated with temperature anomalies at the cold point tropopause (CPT). CPT temperature anomalies as low as -0.8 K during El Niño and as high as 1 K during La Niña phases are possible (*Zhou et al.*, 2001). Figure 1.7 (*Zhou et al.*, 2001) shows signatures of ENSO on

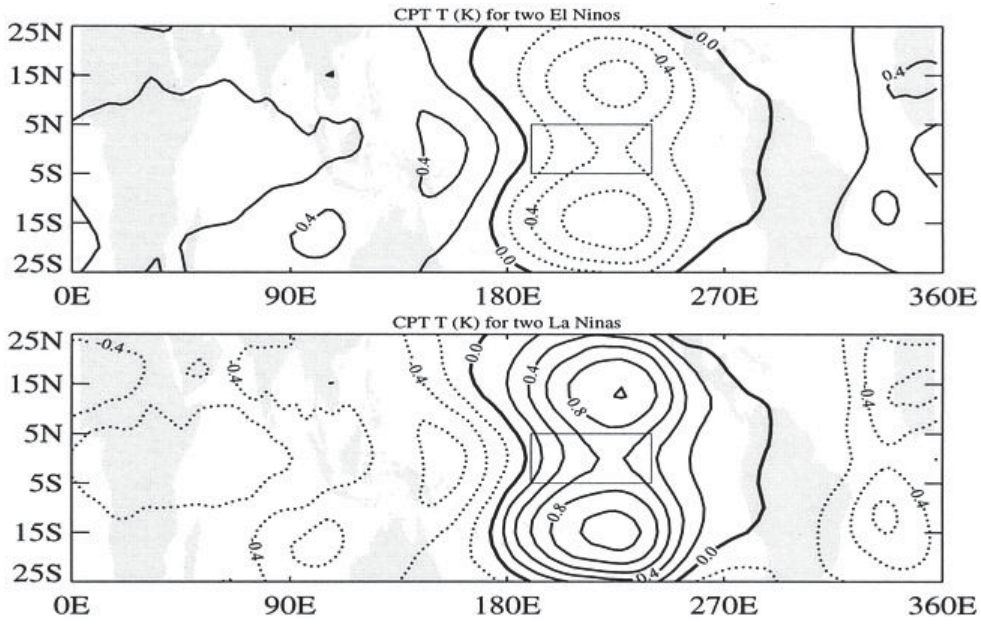

Figure 1.7: Composite analyses of CPT temperatures during two ENSO events that occurred during 1979-93. See the text for the selection of ENSO events. Square boxes show the Niño-3.4 region. Contour interval is 0.20 K. Figure taken from *Zhou et al.* (2001)

CPT temperatures using Niño-3.4 (shown by the rectangular areas) SST anomalies. The authors removed the quasi biennial cycle in these SST anomaly data (eg., *Jiang et al.*, 1995). The frequency overlap of QBO and ENSO has been a problem in the interpretation of low frequency variability in tropopause temperatures and stratospheric entry mixing ratios of tracers. Therefore, the features in Figure 1.7 can be considered due to "uncontaminated" ENSO. The top panel of Figure 1.7 shows a composite of CPT temperature anomalies they constructed using two El Niño's (April 1982- July 1983 and August 1986-February 1988 El Niño's). The bottom panel is the same as the top but using two La Niña's (September 1984- June 1985 and May 1988- January 1989). The most dominant feature of ENSO on these maps is the dumbbell pattern over central eastern Pacific. There are also two more but weaker dumbbells centred around 90^o E and 360^o E. The latter dumbbell forms a dipole pattern with the strongest dumbbell on either side of the equator.

1.3.5 Chemical Tracers of Atmospheric Motion

1.3.5.1 Water vapor (H_2O)

Water vapor is a greenhouse gas with a significant radiative forcing in the stratosphere (*Forster and Shine*, 1999; *Tian et al.*, 2009). Recent changes in its concentration may have contributed to significant changes in global surface temperature (*Solomon et al.*, 2010) . Stratospheric water vapor also regulates the distribution of polar stratospheric clouds, and affects the rate of chlorine catalyzed ozone destruction in polar regions (*Forster and Shine*, 1999; *Tian et al.*, 2009). The mixing ratio of water vapor in the stratosphere is believed to be primarily regulated by temperatures at the tropical CPT. Air parcels are freeze dried as they are vertically advected across the tropopause into the stratosphere, giving rise to an entry stratospheric mixing ratio which is roughly equal to the saturation mixing ratio at the temperature and pressure of the tropopause.

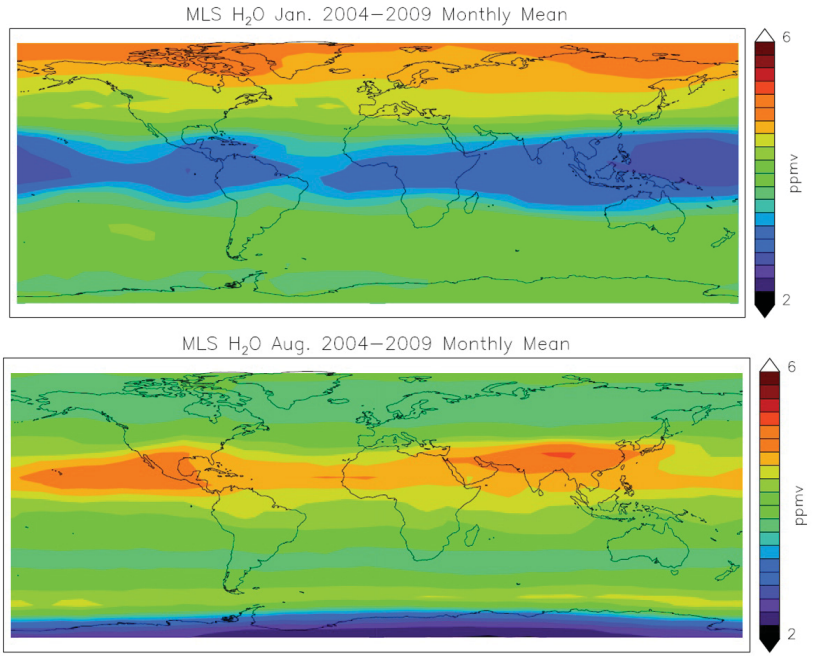

Figure 1.8: Monthly mean water vapor at 82 hPa (∼17.5 km) for (top) January, (bottom) August 2005-2009. Figure taken from *Schoeberl and Dessler* (2011).

1.3.5.2 Seasonal Cycle of H_2O in Ttropical Lower Stratosphere

The seasonal cycle is the dominant source of H_2O variability in the tropical lower stratosphere. In most of the stratosphere, the main player in this cycle is the seasonally changing

meridional circulation strength. The change in strength of this circulation is driven by changes in temperature gradients. Temperatures also directly affect the H_2O seasonal cycle through dehydration processes in the polar regions of winter hemisphere (*Randel et al.*, 2001). Polar dehydration is more common in the Southern Hemisphere where temperatures in the vortex become cold enough. In the tropical tropopause region the H_2O seasonal cycle is a result of interaction between dynamics, local dehydration and convective processes (*Fueglistaler et al.*, 2004; *Steinwagner et al.*, 2010). This multi-phase interaction usually gives rise to a H_2O minimum and maximum during the Northern Hemisphere winter and and summer respectively as shown in Figure 1.8.

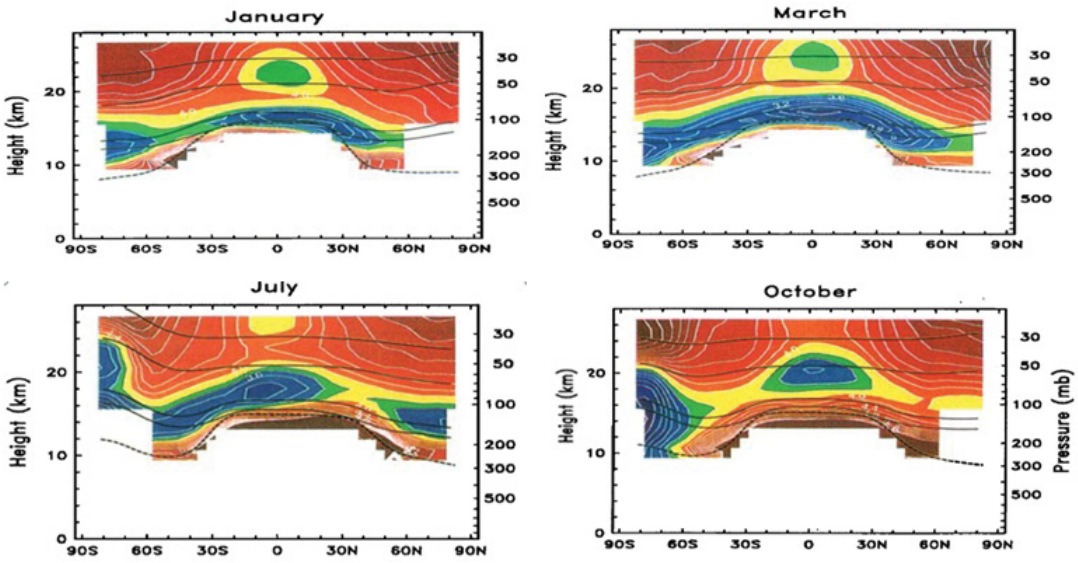

Figure 1.9: Seasonal Cycle of monthly zonal mean H_2O as seen in height-latitude cross-sections. Isentropic levels of 380, 400, 500 and 600 K are shown by solid lines. Dashed lines show tropopause and the white contours are at 0.2 ppmv interval. Taken from (*Randel et al.*, 2001)

Figure 1.9 shows meridional sections of monthly zonal mean water vapor mixing ratios at different heights. The solid lines in each plot are isentropic levels of 380, 400, 500 and 600 K. The dashed lines show the tropopause. In January, the tropical tropopause region is already at its water vapor minimum and the minimum is tilted towards the Northern Hemisphere. This is due to the asymmetry in the strength of BDC which is about two times stronger in the NH winter (*Rosenlof*, 1995). There is also water vapor minimum seen over

Antarctica in the 10-16 km height range. By March, the two minima merge together and in the NH the tropical minimum reaches as far as 75^oN. Vertically, this minimum goes well above the 400 K isentrope in most latitudes at this time of the year. As the year progresses, this minimum migrates upward and southward. During June-October, water vapor near the tropical tropopause region builds up. Above about 500 K surface, the isolation of the tropical stratosphere from high latitude stratosphere can be seen from the sharp contours in both hemispheres. This phenomenon is referred to as a "tropical pipe" (*Plumb*, 1996).

1.3.5.3 Height Time Cross Section of H_2O: The Tropical Tape Recorder

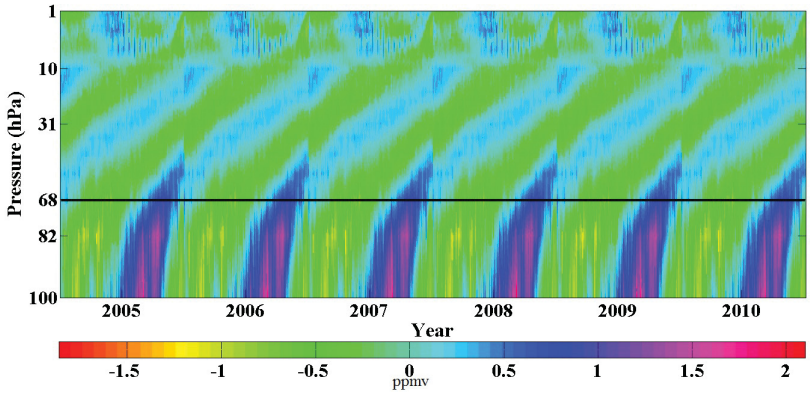

Figure 1.10: Tropical Tape Recorder of H_2O constructed from MLS mean daily H_2O data averaged for the 20^oN- 20^oS minus the mean for the period 2005-2010.

Figure 1.10 shows the upward propagation of MLS H_2O anomalies. It is clearly seen that both the dry and wet anomalies move upward with time as indicated by the tilting to the right of the signals. Although the positive anomalies drop sharply in magnitude, the negative anomalies remain nearly the same in their journey up to about 10 hPa level by the time about 18 months are elapsed. In this figure, we also see the tape recorder of the year 2004 on the left side just above 68 hPa (negative anomaly), and around 30 hPa (positive anomaly). Due to the MLS vertical resolution and sensitivity, the H_2O tape recorder starts around 68 hPa level (shown by solid horizontal line), as can be seen by the level where the anomaly signals start to tilt to the right. Below this level, the signals are nearly normal to the time axis, which means that they are stationary in the vertical sense. Near the 10 hPa pressure level, this tilting tends to vanish. Above the 10 hPa level, there are nearly circular

patches of positive anomalies interrupted by negative anomalies. These are probably due to seasonal changes in CH_4 oxidation.

The strongest evidence that the entry stratospheric water vapor mixing ratio is controlled by the temperature of the cold point tropopause comes from the tropical tape recorder (*Mote et al.*, 1996; *Mote et al.*, 1998). Similar tape recorders have been shown in hydrogen cyanide (HCN) (*Pumphrey et al.*, 2008) and CO (*Schoeberl et al.*, 2008a). The upward mass flux across the tropical tropopause into the stratosphere is roughly twice as large during Northern Hemisphere winter than Northern Hemisphere summer (*Rosenlof*, 1995). The stronger vertical advection during Northern Hemisphere winter gives rise to more intense adiabatic cooling, and contributes to a seasonal cycle at the tropical tropopause in which the mean temperature is roughly 2-5 K colder in winter than in summer (*Fueglistaler et al.*, 2009). The resulting water vapor minimum during Northern Hemisphere winter is vertically advected, with some time delay, into the tropical lower stratosphere.

1.3.5.4 Geographic Locations of Dehydration

Lower stratospheric mixing ratios of water vapor are much smaller than those mixing ratios taken from below the base of TTL (*Dessler and Sherwood*, 2003). Dehydration of air must then take place within the TTL. However, there have been debates on geographic locations and the process which generate the observed dryness of the stratosphere.

Newell and Gould-Stewart (1981) showed, based on 100 hPa level temperature analysis, that the process of dehydration might not take place throughout the tropical tropopause region, but rather in selected regions where the temperatures are lower than the zonal average temperature. This hypothesis was dubbed the "Stratospheric Fountain" hypothesis. The areas identified were over the western tropical Pacific, Indonesia, Malaysia and India during the summer monsoon. *Dessler* (1998) re-examined the "Stratospheric Fountain" hypothesis by using midlatitude stratospheric observations from the period 1994-97 and derived CPT temperatures. Based on the highest entry mixing ratios, he implied that the "Stratospheric Fountain" hypothesis was too restrictive in terms of the tropical longitudes where tropospheric air actually entered the stratosphere. *Zhou et al.* (2001) on the other hand, indicated Dessler's conclusion was valid only during the mid 1990's by showing

a negative trend, (-0.5 K/decade), in the extended version of the same data Dessler used. This means that, prior to the 1990's, zonally averaged tropical cold point temperatures were not sufficiently low enough everywhere to explain the stratospheric entry water vapor ratio.

Balloon data at Boulder Colorado (40^oN) showed $\sim 1\%$/year water vapour trend in the lower stratosphere during 1980's through the early 2000's (*Oltmans et al.*, 2000). If this trend was globally representative, it would be in apparent conflict with the negative temperature trends observed during the same period. This contradiction between the above negative trend in the CPT temperatures during the 1990's and a positive trend in the stratospheric water vapour mixing ratios starting from the 1980's through the early 2000's (*Solomon et al.*, 2010) is an indication of the complexity of dehydration processes in the TTL.

Divergence calculations (*Sherwood*, 2000), on the other hand, suggested some of the areas in the maritime continent might actually be "stratospheric drains" as air masses over these regions on average descend rather than ascend. *Gettelman et al.* (2000) arrived at a similar conclusion based on results from a global chemical transport model. *Holton and Gettelman* (2001) argued that horizontal transport may cause air masses that experienced exceptionally low temperatures over the western tropical Pacific enter the stratosphere at locations, possibly, far away from the temperature minima region which they called it the cold trap.

1.3.5.5 Subseasonal Variations

Water vapor at the tropical tropopause has been shown to exhibit enhanced variance in subseasonal time scales of 30 - 70 days, and 10 - 25 days (*Mote et al.*, 1998). This type of variability becomes visible when the dominant modes, in this case long period variability which account for more than 90% of the total variability, are removed from the data. *Mote et al.* (1998) subjected UARS/MLS H_2O data to wave number-period decomposition and found that those subseasonal time scales of 30 - 70 days are associated with tropical intraseasonal oscillation (TIO, also called MJO) and the 10 - 25 day time scale variability with the Kelvin waves.

1.3.5.6 Multiyear Variations

The stratospheric entry water vapor mixing ratio has been shown to exhibit enhanced variability in response to the QBO (*Randel et al.*,2004; *Zhou et al.*, 2004; *Randel et al.*, 2004; *Fueglistaler and Haynes*, 2005; *Schoeberl et al.*, 2008b). ENSO is associated with changes in tropical lower stratospheric upwelling and water vapor in models (*Garcia and Randel*, 2008; *Randel et al.*, 2009; *Calvo et al.*, 2010).

1.3.5.7 Carbon monoxide (CO)

Tropospheric carbon monoxide (CO) and methane (CH_4) affect the radical chemistry of the troposphere, in part by controlling the amount of hydroxyl (OH) radical. CO promotes, in a NO_x (NO_x= NO+NO_2) rich environment, HO_x (HO_x=OH+HO_2) catalysed tropospheric ozone (O_3) production (*Crutzen and Zimmermann*, 1991). Tropospheric O_3 is both a pollutant and greenhouse gas. The OH reduction which would otherwise destroy more CH_4 allows CO to play an indirect role in global warming. A major single source of tropospheric CO is oxidation by OH of CH_4. Fossil fuel combustion and biomass burning, among others, are also significant CO sources. Most of the tropospheric CO is lost to OH oxidation that gives a mean chemical lifetime of 2 - 3 months (*Seinfeld and Pandis*, 1997; *Jacob*, 1999). The remaining smaller portion of CO splits between soil uptake and transport to the stratosphere. Since CO mixing ratios decrease with height in the lower stratosphere, an increase in its concentration there can often be attributed to an increase in upwelling. It has been shown (*Schoeberl et al.*, 2008a) that CO has a tape recorder similar to the H_2O tape recorder discussed above. However, the CO tape recorder, unlike H_2O tape recorder, is in response to changes in surface emissions and movement of convection relative to major CO source regions (*Wong and Dessler*, 2007; *Schoeberl et al.*, 2008a). The long lifetime of CO and the fact that it is not removed by condensation makes it a good measure of STE processes.

1.3.5.8 Nitrous oxide (N_2O)

Due to its long chemical lifetime (about 144 years) and high radiative absorption efficiency (in units of W m^{-2} $ppbv^{-1}$) nitrous oxide (N_2O) in the atmosphere has a global warming

potential of 289 times that of CO_2 and about 4 times that of CH_4 in a 20 year time horizon (*Forster et al.*, 2007). The primary and natural sources of N_2O to the atmosphere are vegetation/soil and the oceans (*Seinfeld and Pandis*, 1997; *Jacob*, 1999). Anthropogenic sources include biomass burning and use of nitrogen fertilizers. The main sink for N_2O is the stratosphere where most of it photodissociates and a small portion is oxidized by $O(^1D)$ (*Crutzen*, 1995). Each N_2O molecule produces two NO molecules upon oxidation with $O(^1D)$. The NO formed causes catalytic loss of stratospheric O_3 (*Crutzen*, 1995). Therefore, N_2O is as important as an ozone depleting substance (ODS) as it is a strong greenhouse gas. In this thesis, we will be using N_2O as one of the dry atmospheric tracers of motion.

CHAPTER 2

DATA

2.1 Description of Datasets

In this chapter, description of datasets used in the thesis are presented. Measurements of water vapor (H_2O), carbon monoxide (CO), and nitrous oxide (N_2O) are obtained from the Microwave Limb Sounder (MLS) (*Waters et al.*, 2006). Temperature data come from three reanalysis products: (1) ERA-Interim, European Centre for Medium-Range Weather Forecasts (ECMWF) (*Dee and Uppala*, 2009) (2) The National Center for Environmental Prediction (NCEP) (*Kalnay et al.*, 1996) (3) The Modern Era Retrospective Analysis for Research and Application (MERRA) (*Rienecker et al.*, 2008). Also, GPS temperature data from Constellation Observing System for Meteorology, Ionosphere, and Climate, COSMIC (*Anthes et al.*, 2000) are presented. The H_2O measurements from MLS are compared with measurements from the Atmospheric Chemistry Experiment - Fourier Transform Spectrometer (ACE-FTS) instrument (*Bernath et al.*, 2005). The three reanalysis temperature data are compared for 100 hPa level. Data selection and preparation for further analyses are also included.

2.1.0.9 MLS: H_2O, CO and N_2O

The Microwave Limb Sounder (MLS) (*Waters et al.*, 2006) is one of four instruments on the National Aeronautics and Space Administration (NASA) Earth Observing Satellite (EOS) Aura satellite, launched on July 15th 2004. Aura/MLS started taking observations on 13 August 2004. This thesis, however, will focus on the Jan 1, 2005 - Dec 31, 2010 time period. Aura is in a sun-synchronous near-circular polar orbit as a member of the

constellation of satellites called the A train. MLS observes microwave emission from molecules such as H_2O, CO, N_2O in five spectral regions from 118 GHz to 2.5 THz using seven radiometer devices. The altitude range of MLS is from near the ground to ~ 90 km and near global in the horizontal, (82^o S - 82^o N). The MLS can take measurements during the day and night, and in the presence of ice clouds and aerosols that would normally prevent measurements by most other sensors.

This thesis uses MLS level 2, v3.3 H_2O, CO and N_2O measurements (*Waters et al.*, 2006; *Lambert et al.*, 2007; *Read et al.*, 2007; *Vömel et al.*, 2007b). H_2O is reported on 55 pressure levels, while CO and N_2O are reported on 37 pressure levels. The vertical resolution for H_2O ranges between 2.0 to 3.7 km for pressure levels 316-0.22 hPa, while the along track horizontal resolution is $\sim$ 210-360 km for pressures greater than 4.61 hPa. The across track resolution is 7 km for all pressures. In the TTL, the vertical and along track resolutions of the CO measurements are 3.5-5 km and $\sim$ 700 km respectively. The vertical and along track resolutions of the N_2O measurements are 4-6 km and 300-600 km, respectively. Erroneous profiles have been screened using status and quality flags, convergence, and precision fields (*Lambert et al.*, 2007; *Read et al.*, 2007). Profiles with odd status and negative precision outside prescribed quality and convergence fields were rejected. Cloud status fields are more important below the 100 hPa pressure level and were not used (*Lambert et al.*, 2007). Negative values were considered valid, since their rejection would give rise to positive bias in the tropical daily mean averages.

2.1.0.10 ACE: H_2O

The ACE-FTS instrument uses solar occultation (up to 15 sunrises and 15 sunsets occultations per day) technique to obtain vertical profiles of up to 82 species (*Bernath et al.*, 2005). It was launched on the Scientific Satellite-1 (SCISAT-1), and has been taking measurements since January 2004. Version 3.0 water vapor measurements from this instrument are compared with the 68 hPa MLS water vapor measurements. Due to the satellite orbit, ACE-FTS measurements from the tropics are available for about four months per year.

2.1.0.11 ERA-Interim

ERA-Interim is a global atmospheric reanalysis produced by the European Centre for Medium-Range Weather Forecasts, (ECMWF), and is available from 1979 to the present

(*Dee and Uppala*, 2009). Atmospheric model and data assimilation techniques are improved from ERA-40 (*Bouttier and Rabier*, 1997). ERA-Interim has 37 pressure levels and a horizontal resolution of $1.5^o \times 1.5^o$. The four times per day temperature analyses, obtained from the ECMWF website (`http://data-portal.ecmwf.int/data/d/interim_daily/`), are used to calculate daily mean values at 100 hPa for 2005-2010. ERA-Interim is a global analysis and has a coarse vertical spacing near the tropopause. The 100 hPa level is chosen as the level nearest to the tropopause in the 30^o N-30^o S latitude range.

2.1.0.12 NCEP

The National Center for Environmental Prediction (NCEP) (*Kalnay et al.*, 1996) provides a global reanalysis product during the period 1948 - present. The NCEP reanalysis has a horizontal resolution of $2.5^o \times 2.5^o$, and 17 pressure levels. The NCEP 100 hPa reanalysis temperature data were obtained from the NOAA/PSD website (`http://www.esrl.noaa.gov/psd/`).

2.1.0.13 MERRA

The Modern Era Retrospective Analysis for Research and Application, (MERRA), uses NASA's GEOS-5 data assimilation system (GEOS-5 DAS) (*Rienecker et al.*, 2008). The data archive covers the period from 1979-present. The GEOS-5 model has a native resolution of $2/3^o$ longitude by $1/2^o$ degree latitude (*Bosilovich et al.*, 2008; *Rienecker et al.*, 2011) but the daily temperatures are reported on a $1.25^o \times 1.25^o$ grid. The model has 72 vertical levels extending from surface to 0.01 hPa. The 100 hPa temperatures used in this thesis are obtained from the NASA Goddard Earth Sciences Data and Information Services Center (GES DISC) website (`http://mirador.gsfc.nasa.gov/`).

2.1.0.14 COSMIC

Constellation Observing System for Meteorology, Ionosphere, and Climate (COSMIC) (*Anthes et al.*, 2000) is an indirect, yet accurate atmospheric sounding mission providing 1500-2000 atmospheric soundings per day globally. Nearly a quarter of these soundings are taken from the tropics. The high vertical resolution (post processed data interpolated

between 100 m height intervals), high accuracy (< 1 K), self calibrating and all weather sounding capability of the GPS technique (*Anthes et al.*, 2008) make COSMIC data one of the best candidates for diagnosing features like the cold point tropopause temperatures and their heights. COSMIC temperature data for the period 2008-2010 found from the website (http://cosmic-io.cosmic.ucar.edu/cdaac) will be used to produce a map of CPT temperatures.

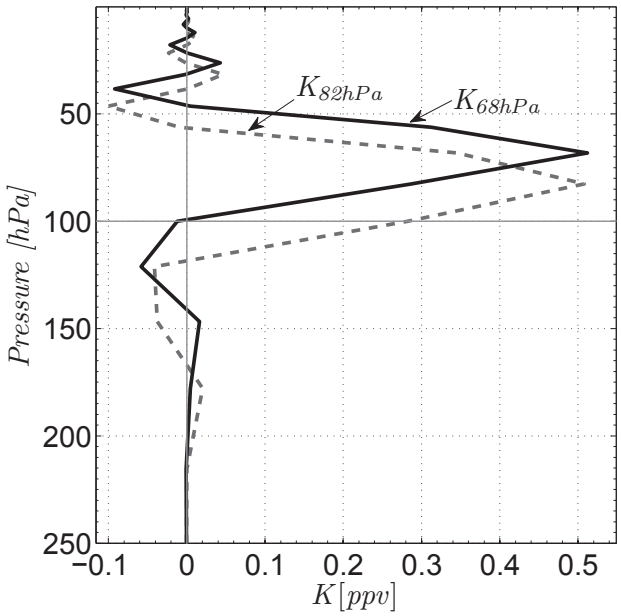

Figure 2.1: Averaging kernels of MLS v3.3 H_2O. Solid line is for 68 hPa and broken line is for 82 hPa pressure level.

2.1.0.15 MJO and QBO/ENSO Indices

The first of the two multivariate MJO indices (RMM1) obtained from the Centre for Australian Weather and Climate Research website (`http://cawcr.gov.au/staff/mwheeler/maproom/RMM/RMM1RMM2.74toRealtime.txt`) are used. RMM1 is the first Principal Component (PC) time series that form the index called the Real-time Multivariate MJO series 1 (RMM1), (*Wheeler and Hendon*, 2004).

Monthly QBO indices come from Climate Prediction Center (CPC) website at National Oceanic and Atmospheric Administration (NOAA) (`http://www.cpc.ncep.noaa.`

gov/data/indices/). The zonally averaged wind index (formally called Singapore winds) anomalies at 30 and 50 hPa are used as proxies for the QBO. Only the 50 hPa component is used to investigate the QBO signature on the temperature field at 100 hPa.

Monthly data for Global Sea Surface Temperature (SST) ENSO indices (defined as the average SST anomaly equatorward of 20^o latitude (north and south) minus the average SST poleward of 20^o) are obtained from the University of Washington website, (http://jisao.washington.edu/data/globalsstenso/).

2.2 Data preparation

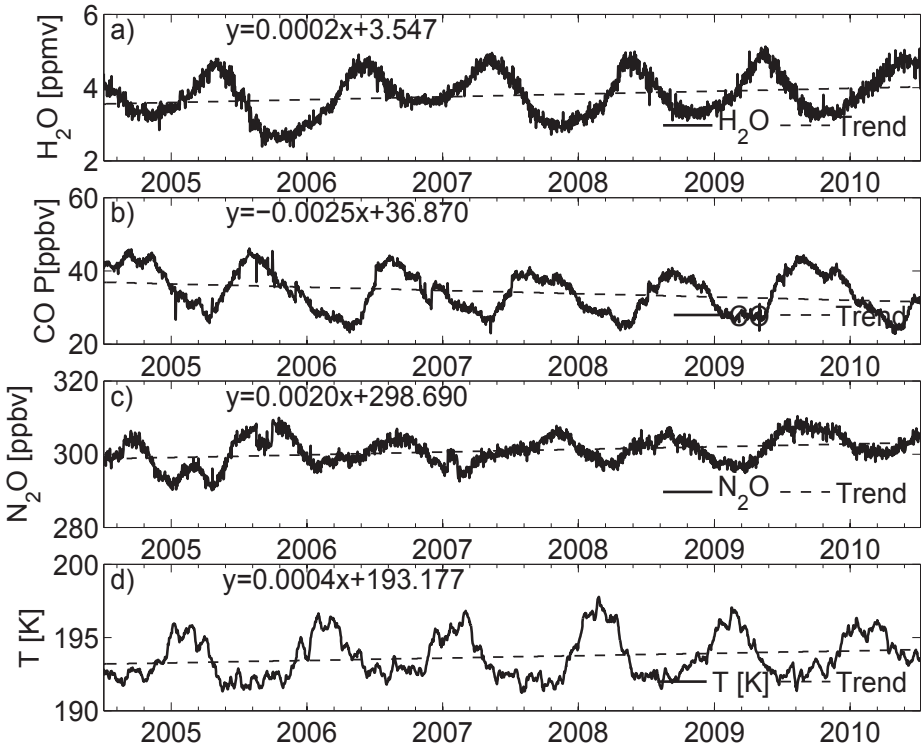

Figure 2.2: Time Series of (a) 15^o N-15^o S averaged 100 hPa MERRA temperature (b) Tropical mean daily values of MLS H_2O, (c) CO and (d) N_2O. Dashed lines are trend lines.

2.2.1 Selection of MLS Pressure Level

Figure 2.1 shows the averaging kernels of v3.3 MLS H_2O measurements on the 82 hPa ($\sim$ 17.7 km) and 68 hPa ($\sim$ 18.8 km) pressure levels, obtained from the MLS webpage (`http://mls.jpl.nasa.gov/data/ak/`). The 82 hPa kernel extends significantly below the 100 hPa level into the troposphere. Although the 68 hPa averaging kernel also has some weighting below 100 hPa, this weighting should be sufficiently small that the MLS measurements on this pressure level are most reflective of the stratospheric entry mixing ratio. Although the MLS averaging kernels are species dependent to some extent, we also use CO and N_2O measurements on the 68 hPa level.

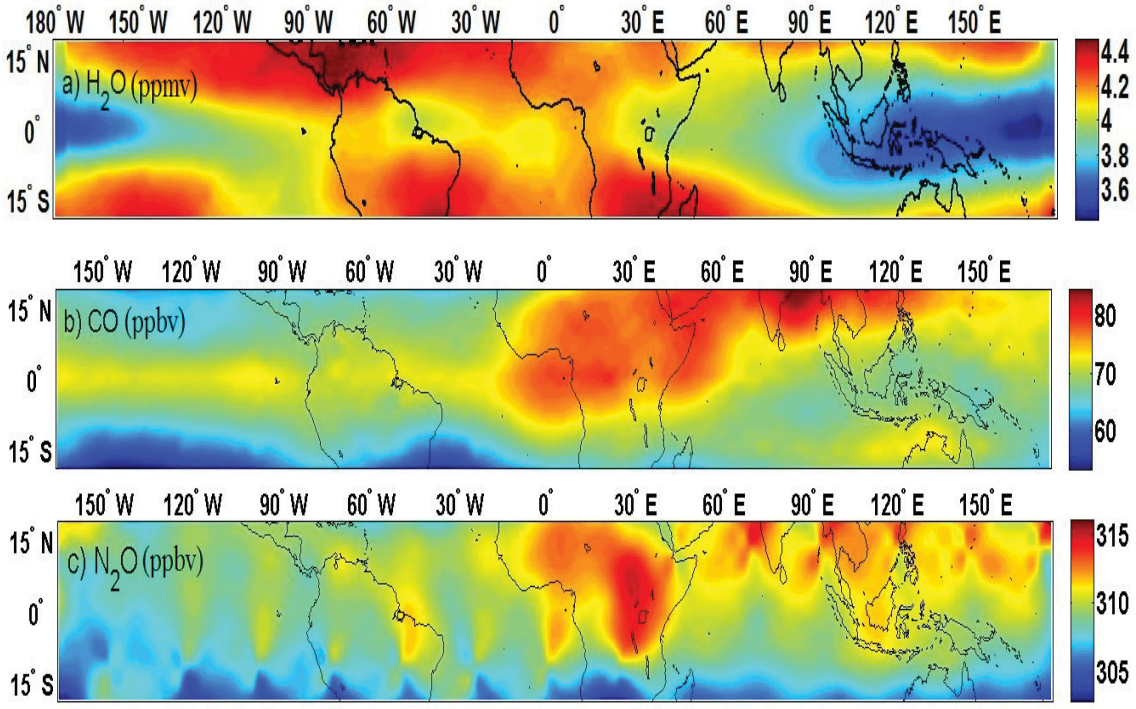

Figure 2.3: 100 hPa MLS 2005-2010 daily climatologies of a) H_2O b) CO and c) N_2O

The 100 - 50 hPa pressure range of the 68 hPa averaging kernel shown in Figure 2.1 corresponds to a height range of roughly 4 km (16.6 - 20.6 km). The annual mean upwelling velocity between 17 and 20 km is roughly 0.25 mm s^{-1} ($\sim$8 km yr^{-1}) (*Randel et al.*, 2008). An air parcel would therefore require about 200 days to vertically traverse the full depth of the MLS averaging kernel. The 68 hPa MLS measurements are therefore

unlikely to capture changes in the stratospheric entry tracer mixing ratio of a chemical tracer on time scales less than a month.

2.2.2 Mean Values (2005-2010)

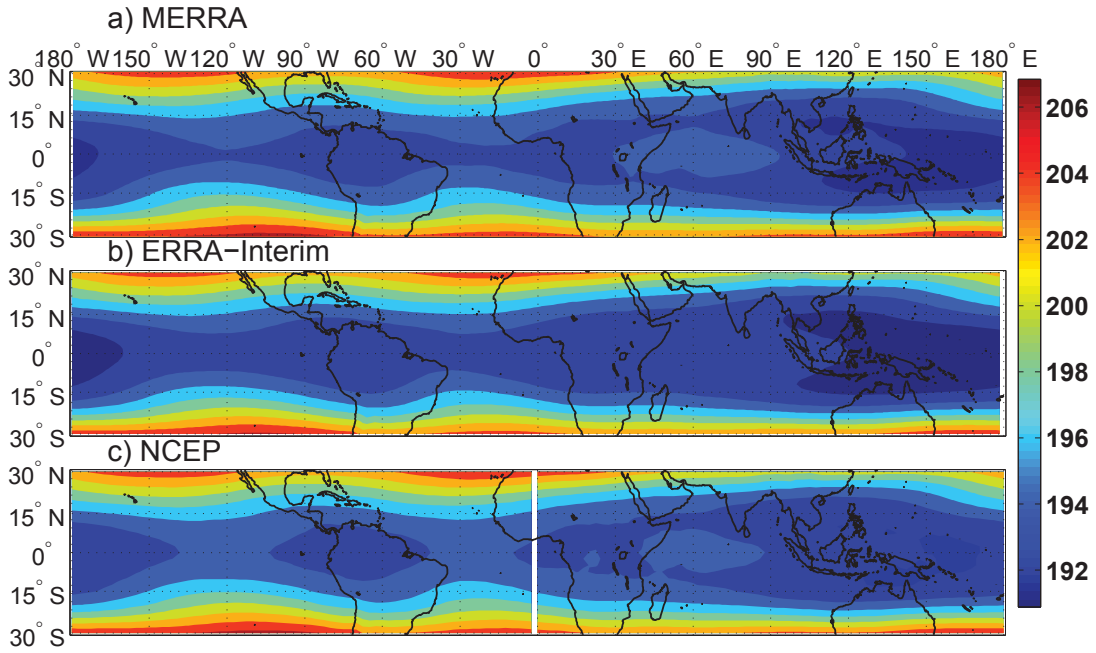

Figure 2.4: Time (2005-2010) averaged 100 hPa daily temperatures (K) a) MERRA b) ERA-Interim and c) NCEP.

Figures 2.2a-c show the variation in tropical mean daily (20^o S - 20^o N) MLS H_2O, CO, and N_2O from 2005 to 2010 on the 68 hPa surface. Figure 2.2d shows the variation of (15^o S -15^o N) mean daily MERRA temperature on the 100 hPa surface. Here only MERRA temperatures are included because eventually this product will be used for further calculations. The dashed lines show the trends in the measurements. During the 2005-2010 period the absolute mean tropical daily values of 68 hPa H_2O, CO, and N_2O were 3.78 ppmv, 34.2 ppbv, and 301.0 ppbv, respectively.

Figures 2.3a-c show the spatial distribution of time averaged (2005-2010) H_2O, CO, and N_2O on 100 hPa surface. To construct these maps irregularly spaced measurements were linearly interpolated into $1.5^o \times 1.5^o$ grids. The method suffered in locations where observational data are scarce. This resulted in some discontinuities in the eastern and western

edges of the CO and N_2O maps. However, the main features of the tracer distributions such as the dry conditions in the maritime continent, the CO maxima over Asia and Africa and the N_2O peak over much of of Africa are well captured.

Figures 2.4a-c show maps of time averaged daily mean 100 hPa temperatures for the period 2005-2010. In all three maps, temperatures are cold in the deep tropics (15^o S -15^o N). In all cases, the temperatures over the maritime continent are the coldest followed by a small colder area over South America. Generally, these maps show strong agreement among the three temperature products. A visual inspection shows ERA-Interim has the coldest temperatures over the western Pacific. NCEP coldest temperatures are the highest of the three in this region. Even though they are small, these differences may affect interpretations of stratospheric H_2O variability and hence we will do a quantitative comparison later on.

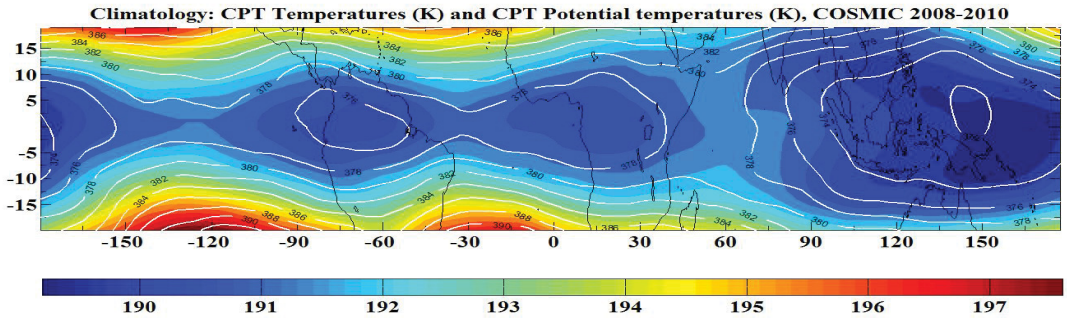

Figure 2.5: COSMIC daily mean temperatures (shaded) and potential temperatures (contours) at CPT. Contour interval=2 K.

Figure 2.5 shows a three year GPS climatology of daily temperatures (shaded) and potential temperatures (white contours) at the CPT. As with the tracers, this map was constructed using $1.5^o \times 1.5^o$ grid interpolation. The relatively dense observation of COSMIC allowed the simple interpolation technique used here to produce the main features without a problem. The zonal asymmetry of the coldest areas is more visible at the CPT than at 100 hPa. Also, note that the lowest potential temperatures (about 4-6 K cooler) are over the western Pacific. This is in agreement with *Seidel et al.* (2001).

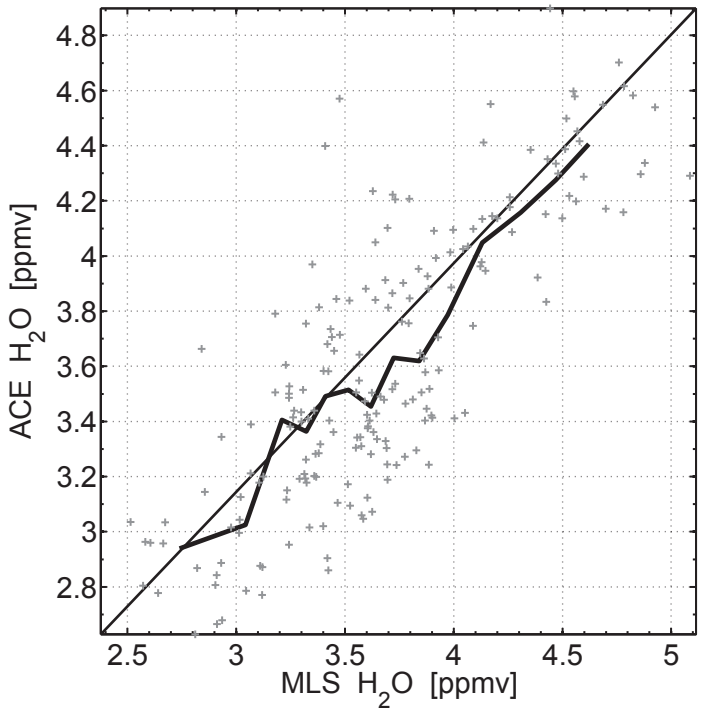

Figure 2.6: A scatter plot of tropical mean (20^o N-20^o S) daily ACE and MLS H_2O at 68 hPa. (ACE H_2O interpolated onto MLS pressure levels)

2.2.3 Data Comparison

2.2.3.1 Water vapor

Figure 2.6 shows a scatter plot of tropical mean daily ACE v3.0 and MLS v3.3 H_2O values at 68 hPa. ACE data from the height range 16.5-19.5 km during the period 2005-2010 are extracted and checked for data quality. ACE data are provided along with statistical error values for each measurement. Measurements whose accompanying statistical errors exceed 10% of the reported data are rejected. ACE has a relatively complete measurement in the tropics during the months of February , April, August, and October only.

This short time coverage and the data quality criterion applied reduced the number of ACE data points with which the comparison with MLS was made. The four ACE grid heights were converted to pressure levels using tropical mean pressures for the conversions. Then, a simple linear interpolation was done to compute ACE H_2O at 68 hPa. The broken line in Figure 2.6 represents the class means of the two data sets when each grouped into

14 bins with a bin size of 0.150 ppmv. Generally, while there is a good correlation between the two data sets ($r = 0.778$), MLS is slightly wetter than ACE as can be seen from the class means line in Figure 2.6.

2.2.3.2 100 hPa Temperatures

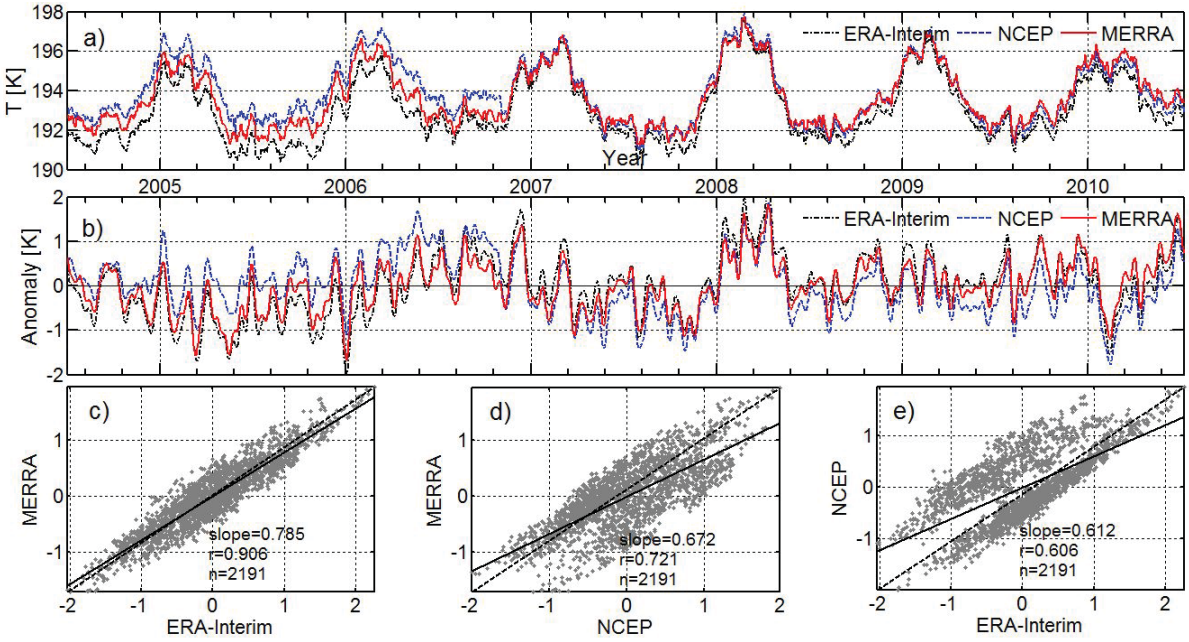

Figure 2.7: Time series, of (a) 15 N-15 S average 100 hPa reanalyses temperatures and (b) deseasonalized, 15-day low pass filtered anomalies of those in (a). Dark dotted line, blue dashed and red solid lines represent ERA-Interim, NCEP, and MERRA. Scatter plots showing comparison of the temperature anomalies of (c) MERRA vs ERA-Interim, (d) MERRA vs NCEP and (e) NCEP vs ERA-Interim. Solid lines represent least square lines whose slopes are shown on lower left.

The dotted, dashed, and solid lines in Figure 2.7a refer to ERA-Interim, NCEP and MERRA 100 hPa temperatures respectively, averaged between 15^o N and 15^o S, from 2005 to 2010. Temperatures from the NCEP reanalysis were roughly 2 K higher than the other two from early-2005 to mid-2007 (*Randel et al.*, 2000; *Wong and Dessler*, 2007). After mid-2007, NCEP temperatures are usually colder than ERA-Interim and MERRA. ERA-Interim and MERRA temperatures are usually in good agreement between 2005 and 2010. Figure 2.7b shows 15-day Lanczos low pass filtered (*Duchon*, 1979) deseasonalized anomalies of the temperature time series shown in Figure 2.7a. This figure shows more

clearly the 2005 to mid-2007 warm bias, and 2008 - 2010 cold bias, of the NCEP reanalyses relative to ERA-Interim and MERRA.

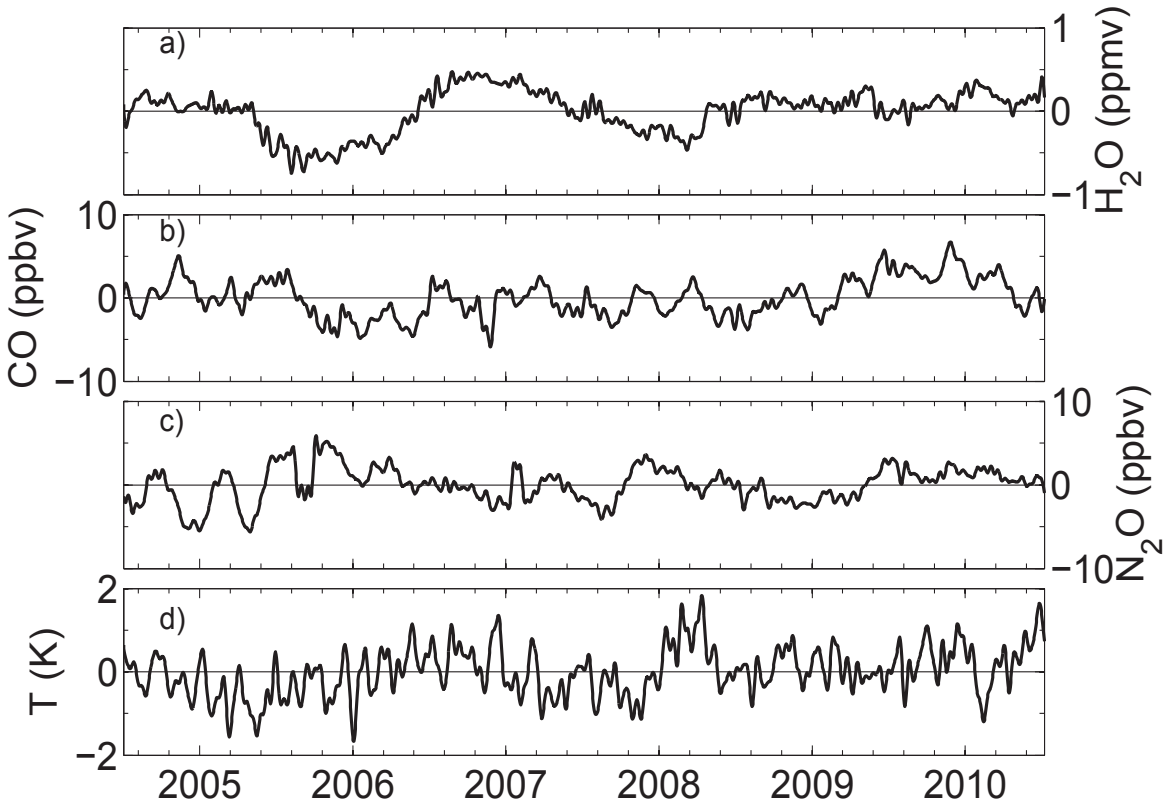

Figure 2.8: Time series of deseasonalized, detrended, 15-day low pass filtered anomalies for time series shown in Figure 2.2: (a) H_2O, (b) CO, (c) N_2O and (d) Temperature.

Figures 2.7c-e show scatterplots of the reanalysis temperature anomalies against one another. The MERRA and ERA-Interim temperature anomalies are in the best agreement, with a correlation $r = 0.906$, and slope $b = 0.785$. The two plots involving NCEP temperature anomalies indicate a tendency for the points to segregate into two groups. This splitting reflects the warm and cold biases of NCEP temperature anomalies in the periods before and after mid-2007 discussed earlier. Given the greater consistency of the MERRA and ERA-Interim reanalyses, and the finer spatial resolution of the MERRA reanalysis, we use MERRA temperatures in our subsequent analysis. However, the results are similar to those obtained using ERA-Interim temperatures.

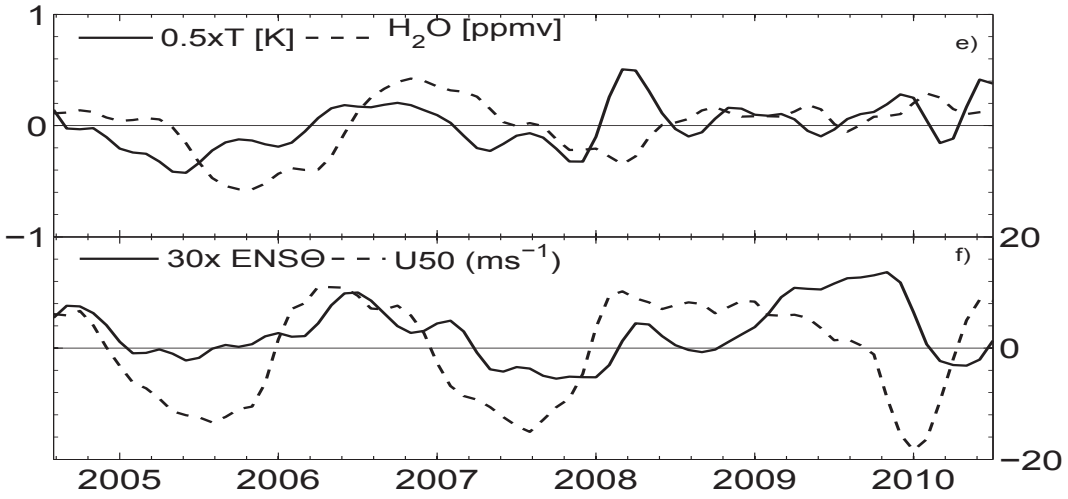

Figure 2.8: continued: (e) Solid and dashed lines represent anomalies of tropical mean monthly MLS H_2O, and 15^o N-15^o S averaged 100 hPa monthly mean MERRA temperatures (f) Solid and dashed lines represent zonal mean 50 hPa wind (U50) anomaly and global ENSO index.

2.2.4 Anomaly Calculations

Figures 2.8a-d show the anomalies in tropical mean H_2O, CO, and N_2O, and temperature, all in the same unit as their absolute values, respectively. The anomalies were calculated from the tropical mean values by removal of the 6 year (2005 - 2010) mean, removal of the seasonal cycle by subtraction of the annual and semi-annual harmonics, and removal of the linear trends. None of the results strongly depends on whether the trend is removed or retained. A 15-day low pass Lanczos filtering is also applied to all daily anomalies.

In Figure 2.8e, the solid and dashed lines refer to anomalies in monthly mean 100 hPa (re-scaled) temperature (15^o N-15^o S) and 68 hPa water vapor (20^o N-20^o S) respectively. From 2005 to early 2009, the water vapor anomalies lag temperature anomalies by several months. The solid and dashed lines of Figure 2.8f refer to monthly mean zonal wind anomalies at 50 hPa (U50) and the ENSO (re-scaled) index respectively. The U50 line shows a periodicity of approximately 2 years. Each of the monthly time series has been smoothed (for plotting purpose only) by applying a 3-month low pass filter.

2.2.5 *Data removal from N_2O time series*

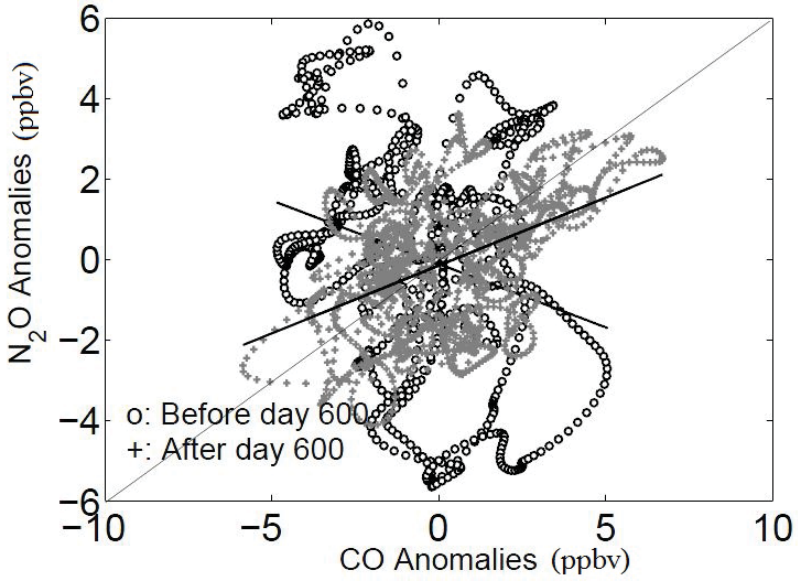

Figure 2.9: Scatter plot of anomalies of CO and N_2O from Figure 2.8: Data pairs before and after the first 600 days of 2191 days shown in dark ”o” and grey ”+” marks. (See the text for slopes of the corresponding least square lines.)

As can be seen in Figures 2.3b-c CO and N_2O have somewhat similar spatial distributions at 100 hPa. Since the dynamics that causes upward transport of both species is the same, one should expect a positive correlation between tropical mean CO and N_2O at 68 hPa. Unfortunately, we do not have a conclusive evidence about this correlation on a spatial and temporal scale this thesis investigated. However, *D'Amelio et al.* (2009) found positive correlations between some of the profiles of CO and N_2O in part of the Amazon during dry seasons and attributed these correlations to biomass burning. In Figure 2.9, the N_2O anomaly is plotted against the CO anomaly for the 2005 - 2010 period. Measurements within the first 600 days are indicated with open circles, while measurements from day 601 to day 2191 are indicated with gray plus signs. N_2O and CO are anticorrelated during the first 600 days with a negative slope b = -0.315 and a correlation r = -0.232. During the remaining time period, N_2O and CO are positively correlated with a positive slope b = 0.426 and r = 0.337. The origin of the change in sign of the correlation is unclear. It may arise from difficulties associated with the definition of the anomalies of the two tracers, and in particular, the parameterization of the seasonal cycle in terms of the two harmonics,

or the assumption that the two species have linear trends. However, because the second part of the N_2O anomaly time series was more consistent with other measurements than the first part, the first 600 days were removed from the N_2O time series.

CHAPTER 3

STATISTICAL METHODS

This chapter outlines the statistical approaches employed in the thesis. The calculation of the coherence between anomalies of tropical (15^o S-15^o N) mean 100 hPa temperatures and anomalies of tropical (20^o S-20^o N) mean 68 hPa mixing ratios of the chemical tracers will be shown as examples of coherence squared calculations. The results will be used to select subseasonal and multiyear time windows for further analyses of the statistical relationships among the anomaly time series.

The main diagnostic used in this thesis is a recently introduced quantity called an average coherence or simply the $\bar{\kappa}$ statistic (*Oliver and Thompson*, 2010). As used here, $\bar{\kappa}$ refers to the standard deviation in the tropical mean mixing ratio of a chemical tracer that can be attributed to the temperature anomalies of a particular grid cell on the 100 hPa surface, normalized by the observed standard deviation of the chemical tracer. The relationship between temperature fluctuations on the 100 hPa surface and the fluctuations in the mixing ratio of a chemical tracer will vary with frequency, depending on the relative importance of the relevant dynamical modes. A simple empirical orthogonal function, EOF, (interchangeably called principal component analysis, PCA) analysis method is presented in an attempt to identify signatures of these dynamical modes on 100 hPa temperatures. Lagged correlation methods will also be used whenever necessary.

3.1 EOF Analysis

EOF analysis is useful for compressing and classification of multivariate data. To do this, one needs to reexpress the data using a new set of variables, which are smaller in number than the original data. By compressing, we mean avoiding redundancy of information. Redundancy could be measured by the observed correlation (co-variance) within the data.

Let us call our gridded anomaly data matrix $\mathbf{X}'$, which has N×K dimensions, where, N=2191 is the number of anomaly data at each grid box during the six year period, and K=14400 is the number of grid boxes of MERRA temperature field. We use a variance-covariance matrix to solve for the principal components (PC's) of $\mathbf{X}'$. The variance-covariance matrix, $\mathbf{S}$, of $\mathbf{X}'$ is defined as:

$$\mathbf{S} = \frac{\mathbf{1}}{\mathbf{N-1}}\mathbf{X'^{T}X'} \tag{3.1}$$

Where, $\mathbf{X'^{T}}$ is the transpose of the data matrix, $\mathbf{X}'$, and N is as defined above.

Properties of $\mathbf{S}$:

(1) It is a square symmetric N×N matrix

(2) Diagonal elements are sample variances of the N measurements in each grid box

(3) Off diagonal elements are sample co-variances of data from different grid boxes

Since we want to reduce redundant information in the data $\mathbf{X}'$, we diagonalize $\mathbf{S}$. Let us call the diagonalized matrix $\mathbf{S^d}$. The diagonal elements of $\mathbf{S^d}$ are its eigenvalues. These eigenvalues will have their corresponding eigenvectors, which are called the principal components (PC's) of $\mathbf{X}'$. Usually, we extract the eigenvalues, sort in descending order and put them in a column matrix. The first entry of this matrix will contain the highest fraction and the last one will have the least fraction of variance of $\mathbf{X}'$. The eigenvectors are also simultaneously sorted with the eigenvalues so that the first principal component will be associated with the highest fraction of the variance of $\mathbf{X}'$. One can chose the first few PC's to investigate most of the variability in the data $\mathbf{X}'$ by projecting it along these PC's. To project the data $\mathbf{X}'$ along the n^{th} PC, we use the formula.

$$\mathbf{EOF(n) = PC(n)^T X'}, \qquad \mathbf{n = 1, ..., N} \tag{3.2}$$

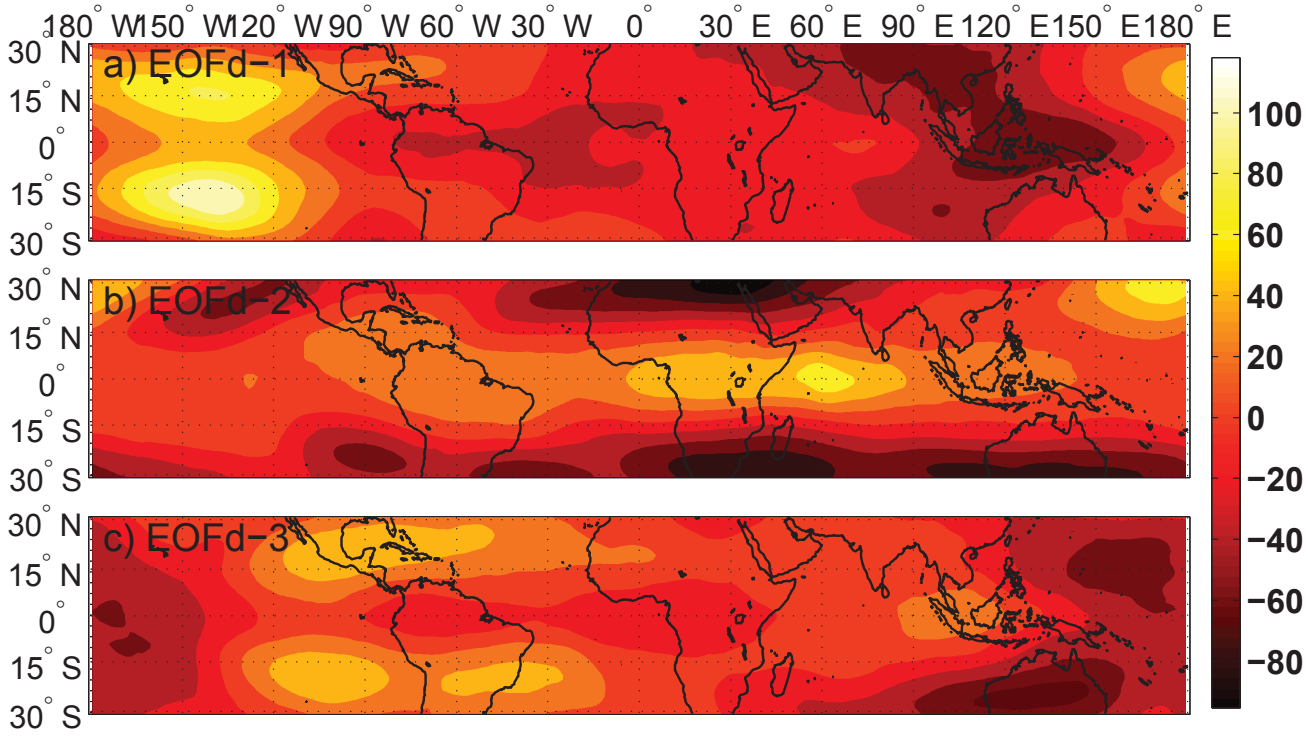

Figure 3.1: The first three EOF's (in units of K^2) of MERRA 100 hPa deseasonalized temperature anomalies. Here, we used daily data for the period 2005-2010.

It is useful to assess the main features within a given dataset in order to best interpret the results of a coherence analysis. For this purpose an empirical orthogonal function (EOF) analysis is done to show the dominant and independent features one can find within the deseasonalized anomalies of 100 hPa gridded temperature data. Note that we just switched to scalar notation of EOF. Here, we calculate the first three EOF's for both mean daily and mean monthly values obtained by averaging the daily values. To avoid confusion, we label EOF's of daily mean temperatures as EOFd, and those of monthly mean temperatures as EOFm. Figures 3.1a shows the first EOF of daily mean temperatures, EOFd-1. One of the main features here is the dumbbell-shaped maxima over the central eastern Pacific. The

boomerang pattern of minima over the maritime continent forms the east-west dipoles with the dumbbell-shaped maxima. These two features are signatures of ENSO on tropopause temperature as discussed in chapter 1. EOFd-1, EOFd-2, and EOFd-3 each explain 9.4%, 8.5%, and 6.1% respectively of the total variance in the deseasoanlized anomaly of daily data.

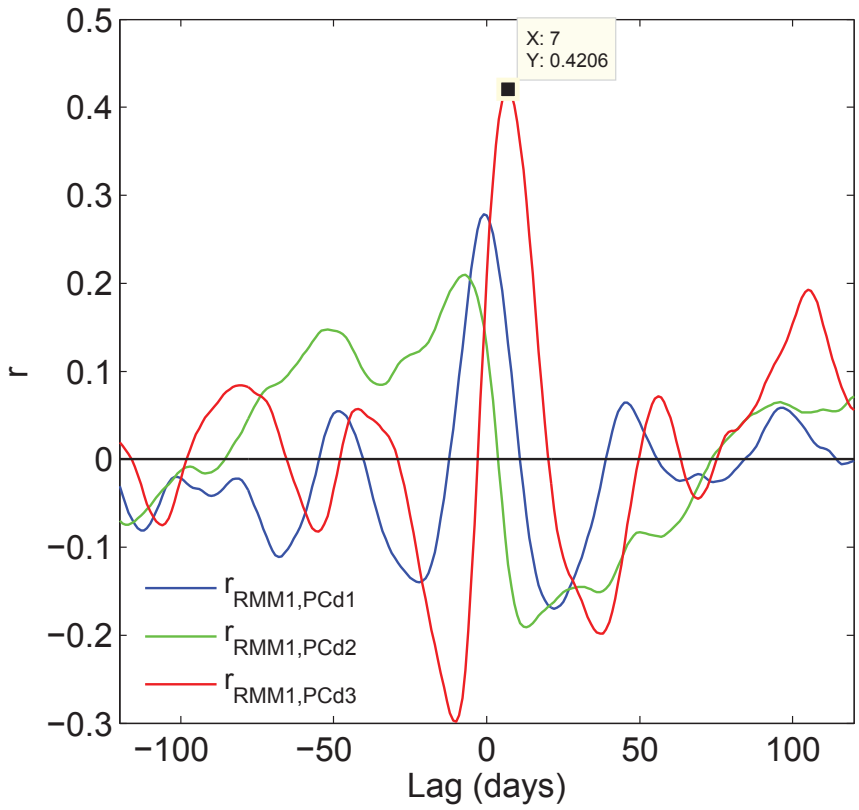

Figure 3.2: Correlations of the first three PC's of deseasonalized anomalies of daily mean MERRA 100 hPa temperatures(PCd's) with RMM1. $r_{RMM1,PCd-1}$, $r_{RMM1,PCd-2}$, and $r_{RMM-1,PCd-3}$ represent correlations of the index RMM1 with the PCd's calculated from deseasonalized mean daily anomalies.

EOFd-3 shows a weaker feature of EOFd-1 with the dipoles shifted to the east. It has been shown that both EOFd-1 and EOFd-3 have relationships to ENSO (*Trenberth and Smith*, 2006). The boomerang minima patterns in both EOFd-1 and EOFd-3 maps extend to the subtropics. These patterns are at the same location as the pair of anticyclones associated with off-equatorial Rossby waves. The zonally symmetric pattern of EOFd-2

might be the QBO signature on the tropopause temperatures (*Randel et al.*, 2000; *Zhou et al.*, 2001; *Zhou et al.*, 2004).

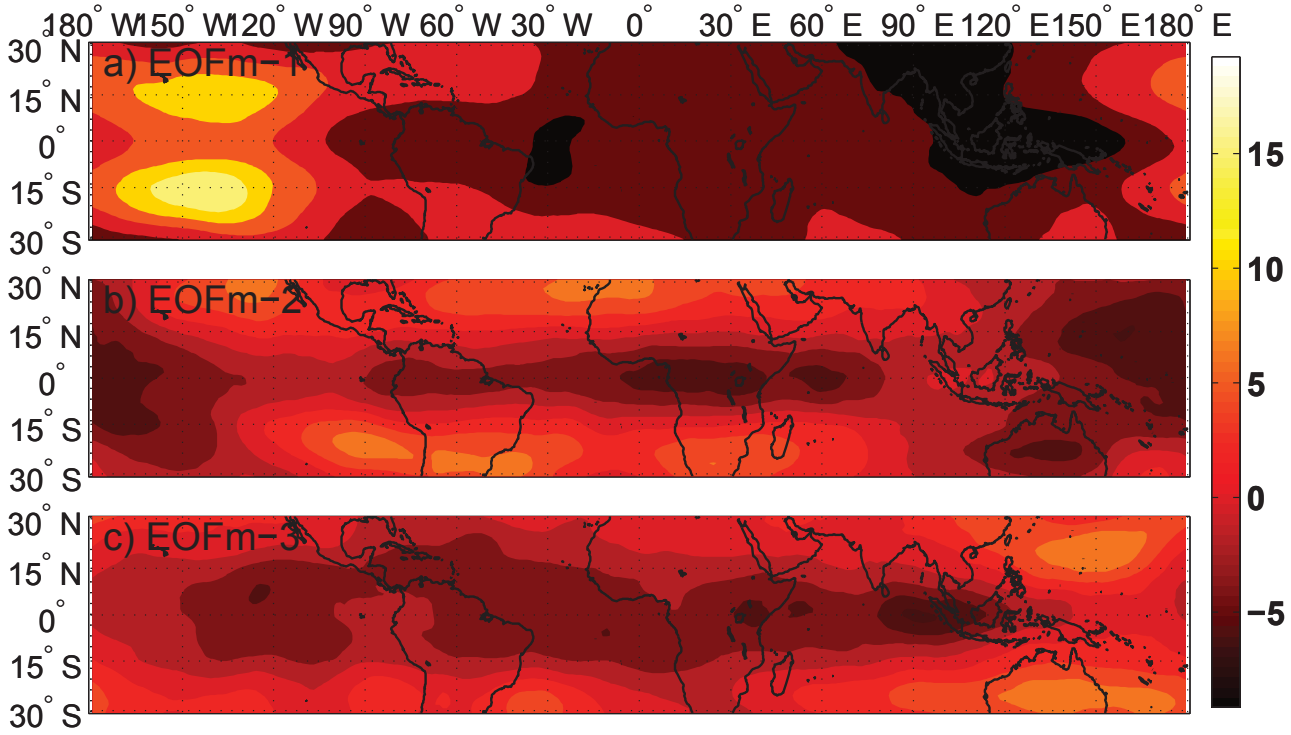

Figure 3.3: The first three EOF's (in units of K^2) of MERRA 100 hPa deseasonalized temperature anomalies. Here, we used monthly averaged data for the period 2005-2010.

One way to look at the link between an EOF pattern with a specific dynamical mode is calculating the correlations between the principal components (PC's) associated with each EOF mode and the index of the dynamical mode. To do this, since the QBO and ENSO indices are usually found in a monthly mean basis, we calculate EOF's and PC's based on monthly averaged 100 hPa temperatures. Again to avoid confusions, we refer PC's associated with daily values as PCd's and those associated with monthly mean values as PCm's. Before we move to monthly calculations, we compute the lagged correlation between one of the MJO indices (RMM1) and the three EOFd's. RMM1 shows the highest correlation (0.42) with EOFd-3 at a lead time of 7 days. This is shown in Figure 3.2.

Figure 3.3 shows the first three EOF's of 100 hPa MERRA deseasonalized mean monthly

temperature anomalies . EOFm-1 explains $\sim 29\%$ of the total variance in the anomaly data. The dumbbell-shaped maxima over central eastern Pacific is still present EOFm-1 map. However, the boomerang minima pattern seen in EOFd-1 (Figures 3.1a) is more diffused here. As a result, the dipole pattern is barely seen. EOFm-2 and EOFm-3 resemble to each other and are nearly zonally symmetric except in the Pacific. EOFm-2 and EOFm-3 each contain $\sim 11\%$ and $\sim 8.8\%$ of the total variance in the monthly anomaly data. The variance explained by EOFm-1 is more three times than EOFd-1. This could be due to averaging of short time scale variabilities in the monthly mean calculation. In the case of daily means, the total variance is spread among several fast modes of variability. However, in terms of the main patterns both daily and monthly EOF's show major features in the 100 hPa temperatures.

In order to confirm whether EOFm-1 pattern is associated with ENSO, we computed the lagged correlations of PCm-1 and global ENSO index. It turns out that PCm-1 is highly anticorrelated with the global ENSO index at zero lag (Black dashed line Figure 3.4). We also, averaged the PCd's to form monthly time series and called the results PCdm's. The lagged correlations of these time series with the ENSO index are plotted in solid lines in Figure 3.4. The blue line ($r_{ENSO,PCdm-1}$) in Figure 3.4 represents the correlations between the monthly mean of PCd-1, called PCdm-1, and the ENSO index. As can be seen from this figure, the correlations of the ENSO index with the first PCm and monthly average of the first PCd are the same. This not true for the higher modes.

3.2 Coherence Squared, κ^2

To calculate the coherence squared (κ^2) between anomalies in 68 hPa tropical mean MLS H_2O and tropical mean 100 hPa 15^o N - 15^o S MERRA temperature, we first define the auto-covariance functions of temperature, γ_T, water vapour, γ_{H_2O}, and the cross-covariance function, γ_{T,H_2O}, (e.g. *Hans and Francis*, 2003).

$$\gamma_T(\tau) = \frac{1}{N-1}\sum_{t=1}^{N}(T(t))(T(t+\tau)) \tag{3.3a}$$

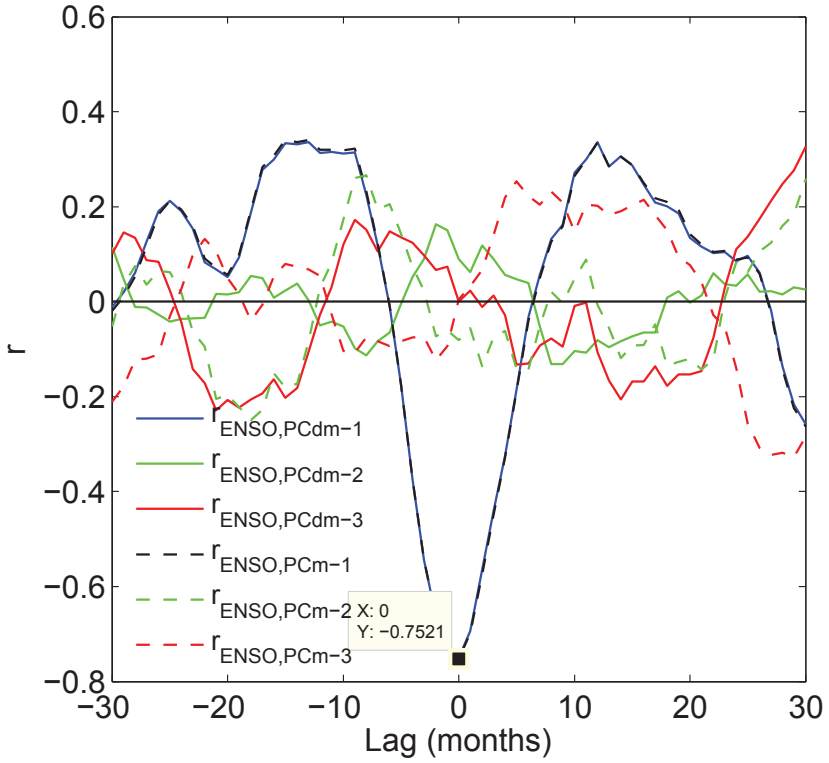

Figure 3.4: Correlations of the first three PC's of MERRA 100 hPa deseasonalized temperature anomalies with global ENSO index. $r_{ENSO,PCdm-1}$, $r_{ENSO,PCdm-2}$, and $r_{ENSO,PCdm-3}$ represent correlations of the index with monthly PC's averaged from daily PC's. $r_{ENSO,PC1-}$, $r_{ENSO,PC-2}$ and $r_{ENSO,PC-3}$ represent correlations of the index with PC's calculated from mean monthly data.

$$\gamma_{H_2O}(\tau) = \frac{1}{N-1}\sum_{t=1}^{N}(H_2O(t))(H_2O(t+\tau)) \tag{3.3b}$$

$$\gamma_{T,H_2O}(\tau) = \frac{1}{N-1}\sum_{t=1}^{N}(T(t+\tau))(H_2O(t+\tau)) \tag{3.3c}$$

N refers to the total number of days, $T(t)$ and H_2O(t) to the temperature and water vapor anomaly daily time series from Figure 2.8b, and τ to a specified time lag. When $\tau = 0$, the auto-covariance functions γ_T and γ_{H_2O} reduce to the variances σ_T^2 and $\sigma_{H_2O}^2$, while the cross-covariance function, γ_{T,H_2O}, is reduced to the covariance σ_{T,H_2O}^2.

For all frequencies $\omega \in [-\frac{1}{2}, \frac{1}{2}]$ (in units of cycles per day), the $\gamma' s$ are then Fourier transformed to give the individual power spectra $\Gamma_T(\omega)$, $\Gamma_{H_2O}(\omega)$, and the cross-spectrum,

$\Gamma_{T,H_2O}(\omega)$ (*Priestley*, 1981).

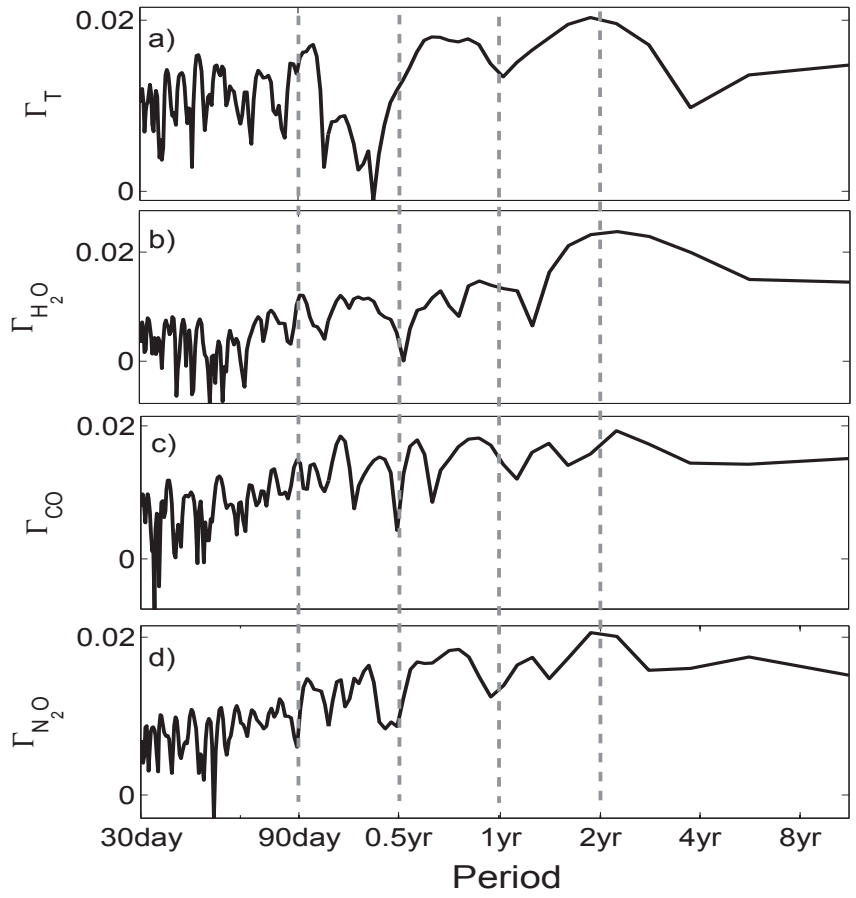

Figure 3.5: Power spectra (unitless) as function of period (in units of day and year (yr)) for 15 day filtered (a) 100 hPa MERRA temperature anomalies (15^o S-15^o N mean) and 68 hPa MLS (b) H_2O, (c) CO, and (d) N_2O anomalies (20^o N-20^o S mean).

$$\Gamma_T(\omega) = \sum_{\tau=-\infty}^{\infty} \gamma_T(\tau)\, e^{-2\pi\, i\tau\omega} \tag{3.4a}$$

$$\Gamma_{H_2O}(\omega) = \sum_{\tau=-\infty}^{\infty} \gamma_{H_2O}(\tau)\, e^{-2\pi\, i\tau\omega} \tag{3.4b}$$

$$\Gamma_{T,H_2O}(\omega) = \sum_{\tau=-\infty}^{\infty} \gamma_{T,H_2O}(\tau)\, e^{-2\pi\, i\tau\omega} \tag{3.4c}$$

Figure 3.5 shows the power spectra of the temperature and tracer anomalies. Each power spectrum has been normalized by the number of daily values (N) and the appropriate

variance. Due to the removal of the annual and semi annual cycles, the spectra exhibit minima near periods of 0.5 year and 1 year. The temperature and H_2O power spectra have strong QBO features. The N_2O spectrum has a weaker QBO feature. All tracer spectra exhibit variability within the MJO window (30 - 90 days), but the power is usually weaker than at longer periods.

The cross-spectrum, $\Gamma_{T,H_2O}(\omega)$, can be expressed in a polar coordinate form as

$$\Gamma_{T,H_2O}(\omega) = A_{T,H_2O}(\omega)e^{i\Phi_{T,H_2O}(\omega)} \tag{3.5}$$

where A_{T,H_2O} and Φ_{T,H_2O} are the amplitude and phase spectra respectively. The amplitude spectrum can then be used to define the coherence squared between temperature and water vapor.

$$\kappa^2_{T,H_2O}(\omega) = \frac{A^2_{T,H_2O}(\omega)}{\Gamma_T(\omega)\Gamma_{H_2O}(\omega)} \tag{3.6}$$

The squared coherence $\kappa^2_{T,H_2O}(\omega)$ reduces the complex valued cross-spectrum function, $\Gamma(\omega)_{T,H_2O}$ to a real-valued function of frequency. $\kappa^2_{T,H_2O}(\omega)$ is constrained to have a value between 0 and 1, with 0 indicating an absence of coherence, and 1 indicating the maximum possible coherence.

Figure 3.6a shows the coherence squared κ^2_{T,H_2O} between tropical mean 68 hPa H_2O and 100 hPa MERRA temperature. There is a strong narrow peak within the MJO band (*Zhang*, 2005) centered at 82 days, and a broad maximum at periods longer than 2 years. The width of this maximum suggests that multiyear variability in tropical mean 100 hPa temperature anomalies gives rise to a similar response in water vapor, whether the temperature forcing comes from the QBO or has some other dynamical origin (e.g. ENSO).

Figure 3.6b shows the coherence squared of tropical mean 68 hPa CO and N_2O with 100 hPa MERRA temperature. CO has a significant coherence with temperature in the MJO window, where there are three distinct peaks. N_2O also exhibits peaks within the MJO window, in addition to coherence on multiyear timescales.

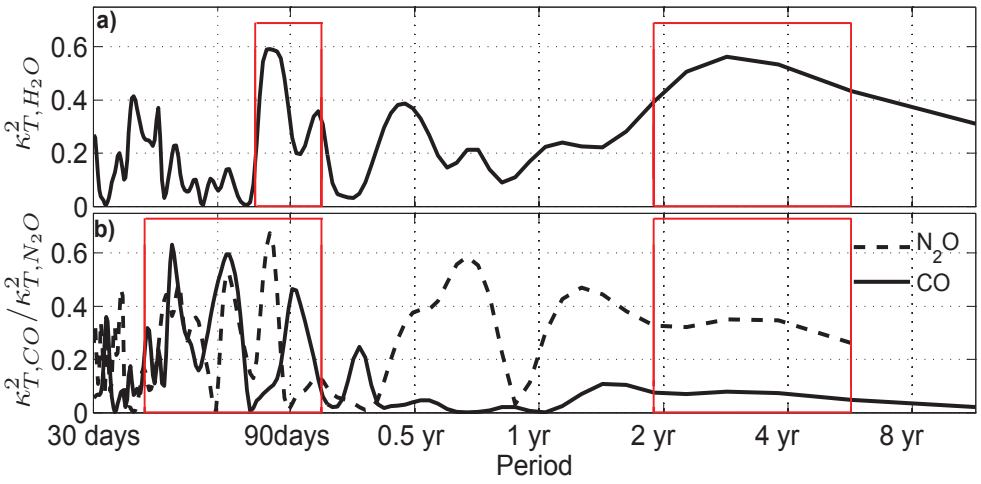

Figure 3.6: Coherence squared (unitless) vs period (in units of days and year (yr)) curves for 15 day filtered 100 hPa MERRA temperature anomalies (15^o S-15^o N mean) and a) H_2O; b) CO (solid line) and N_2O (dashed line). The red boxes indicate the seasonal and multiyear time windows used for the various tracers.

3.3 The $\bar{\kappa}$ Statistic

3.3.1 Derivation

The observed variance of water vapor ($\sigma^2_{H_2O}$) over a given frequency window $[\omega_1, \omega_2]$ can be calculated from the power spectrum Γ_{H_2O}.

$$\sigma^2_{H_2O} = \int_{\omega_1}^{\omega_2} \Gamma_{H_2O}(\omega) d\omega \tag{3.7}$$

The portion of the variance in water vapor that can be attributed to (or "predicted" by) temperature is given by (*Priestley*, 1981),

$$\sigma^2_p = \int_{\omega_1}^{\omega_2} \kappa^2_{T,H_2O}(\omega) \Gamma_{H_2O}(\omega) d\omega \tag{3.8}$$

The $\bar{\kappa}$ statistic is defined as the square root of the predicted variance normalized by the

observed variance (*Oliver and Thompson*, 2010).

$$\bar{\kappa}_{T,H_2O} = \sqrt{\frac{\sigma_p^2}{\sigma_{H_2O}^2}} \tag{3.9}$$

CHAPTER 4

RESULTS AND DISCUSSIONS

4.1 Discussion of BLN Mechanism

Convective heating along the equator generates a characteristic boomerang pattern in dynamical anomalies, with Rossby lobes extending westward from the heat source on both sides of the equator (*Gill*, 1980; *Hendon and Salby*, 1994; *Jin and Hoskins*, 1995; *Ting and Yu*, 1998; *Tian et al.*, 2006; *Ryu and Lee*, 2010). This Rossby wave pattern, and its induced lower stratospheric upwelling, evolve over a roughly 16 days period subsequent to the onset of convective heating at the equator (*Ryu and Lee*, 2010). In the lower stratosphere, fluctuations in upwelling associated with the BLN mechanism will occur at a variety of frequencies, depending on the variance in the generation of Rossby waves by tropical convection. For tracers with vertical gradients, changes in upwelling introduce modifications in the local tendency for vertical advection. The tracer anomalies themselves can therefore be expected to be out of phase with the upwelling anomalies. If changes in lower stratospheric upwelling can be regarded as roughly in phase with 100 hPa temperature anomalies, tracer anomalies from the BLN mechanism should lag 100 hPa temperature anomalies. If the phase offset between lower stratospheric tracer anomalies and 100 hPa temperature anomalies is independent of frequency, the time interval between the 100 hPa temperature anomalies and the response of a lower tropospheric tracer should increase with the period of the upwelling anomaly.

In the case of water vapor, there is a second mechanism through which changes in upwelling can be expected to generate anomalies in the lower stratosphere. An upwelling

increase at the tropical tropopause will increase the rate of adiabatic expansion cooling. In this case, air parcels being advected horizontally and vertically through the TTL will be exposed to colder temperatures, and a greater frequency of dehydration events. Due to the slow ascent rates of the lower stratosphere (*Randel et al.*, 2008), the time lag associated with the appearance of negative water vapor anomalies in the lower stratosphere will be considerably longer than time lag discussed above in association with wave induced changes in vertical advection. This difference in time lags, between the onset of temperature fluctuations on the 100 hPa surface and the occurrence of a water vapor anomaly in the lower stratosphere, provides a method for helping attribute the origin of water vapor anomalies in the lower stratosphere to a particular physical mechanism.

4.2 Spatial Patterns in $\bar{\kappa}$

The definition of $\bar{\kappa}$ given in Eq. 3.9 is used to to calculate the fraction of the variance in the tropical mean 68 hPa mixing ratio of a chemical tracer that can be attributed to MERRA temperature fluctuations at individual grid cells on the 100 hPa surface. The spatial pattern of a $\bar{\kappa}$ map will depend on the time window over which it is defined. We calculate $\bar{\kappa}$ using particular frequency windows in Eqs. (3.7) and (3.8). These frequency windows were chosen by inspection from Figure 3.6, where they are indicated by red boxes.

4.2.1 Subseasonal Time Window

The upper panel of Figure 3.6 shows that the coherence between tropical mean 68 hPa water vapor and 100 hPa MERRA temperature is enhanced in the 74 - 107 days time window. Figure 4.1a shows the H_2O $\bar{\kappa}$ map generated using this subseasonal time window. The most prominent features of this map are two arcs of high $\bar{\kappa}$ on both sides of the equator straddling the western Indian Ocean and Africa, and appearing to originate from a location near the equator west of Indonesia. These high $\bar{\kappa}$ features resemble the lobes of enhanced Rossby wave activity generated by convective heating at the equator. The increased upwelling associated with the breaking of these waves would be expected to generate variability in lower stratospheric water vapor (*Ryu and Lee*, 2010). The main source of convective variance in the 74 - 107 days time window used here to generate the

$\bar{\kappa}$ map is the MJO. One would therefore expect the Rossby patterns here to reflect MJO activity. On the 100 hPa surface, MJO activity in the Indian Ocean is associated with a pair of anticyclones at opposite sides of the equator in the northern and southern Indian Ocean, similar to the patterns shown here in Figure 4.1a (*Weare*, 2010).

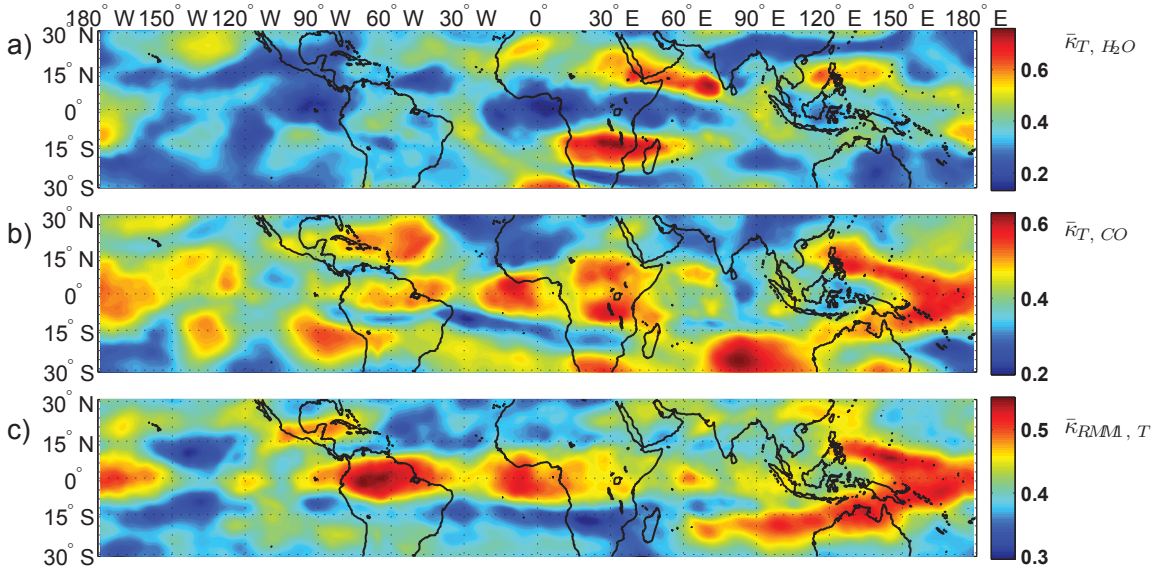

Figure 4.1: $\bar{\kappa}$ maps for subseasonal time windows : a) $\bar{\kappa}_{T,H_2O}$, b) $\bar{\kappa}_{T,CO}$, c) $\bar{\kappa}_{RMM1,T}$.

Figure 3.6b shows the 40-107 days subseasonal time window selected for the CO $\bar{\kappa}$ map. The N_2O $\bar{\kappa}$ map appeared to be noise and is not shown. The CO $\bar{\kappa}$ map shown in Figure 4.1b does, however, appear to exhibit MJO related features. Figure 4.1c shows the $\bar{\kappa}$ map generated from 100 hPa temperature fluctuations and the RMM1 MJO index time series. The RMM1 $\bar{\kappa}$ map shows a boomerang or horseshoe shaped feature (*Nishimoto and Shiotani*, 2012) of high $\bar{\kappa}$ extending from the western equatorial Pacific, with what again appears to be symmetric Rossby lobes extending to the west. The CO subseasonal $\bar{\kappa}$ map (Figure 4.1b) also shows a boomerang feature at the same location. In both patterns, the region of enhanced $\bar{\kappa}$ extends eastward along the equator to 150 E. The CO and RMM1 $\bar{\kappa}$ maps also show similar features over Africa and South America.

4.2.2 *Multiyear Time Window*

Figure 3.6 shows that, on multiyear timescales, the coherence between tropical mean temperatures at 100 hPa and tracer mixing ratios at 68 hPa varies very slowly with period. For the calculation of the $\bar{\kappa}$ maps on multiyear timescales, we therefore selected an identical 682 - 2048 days time window for all three tracers. The H_2O, CO, and N_2O $\bar{\kappa}$ maps associated with this time window are shown in Figures 4.2a, c, d. In general, the $\bar{\kappa}$ maps generated using the multiyear time window show no resemblance to the corresponding $\bar{\kappa}$ maps using the subseasonal time window. The dynamical mechanisms which regulate the transport of chemical tracers into the stratosphere on multiyear timescales are clearly different from the mechanisms which control this transport on subseasonal timescales.

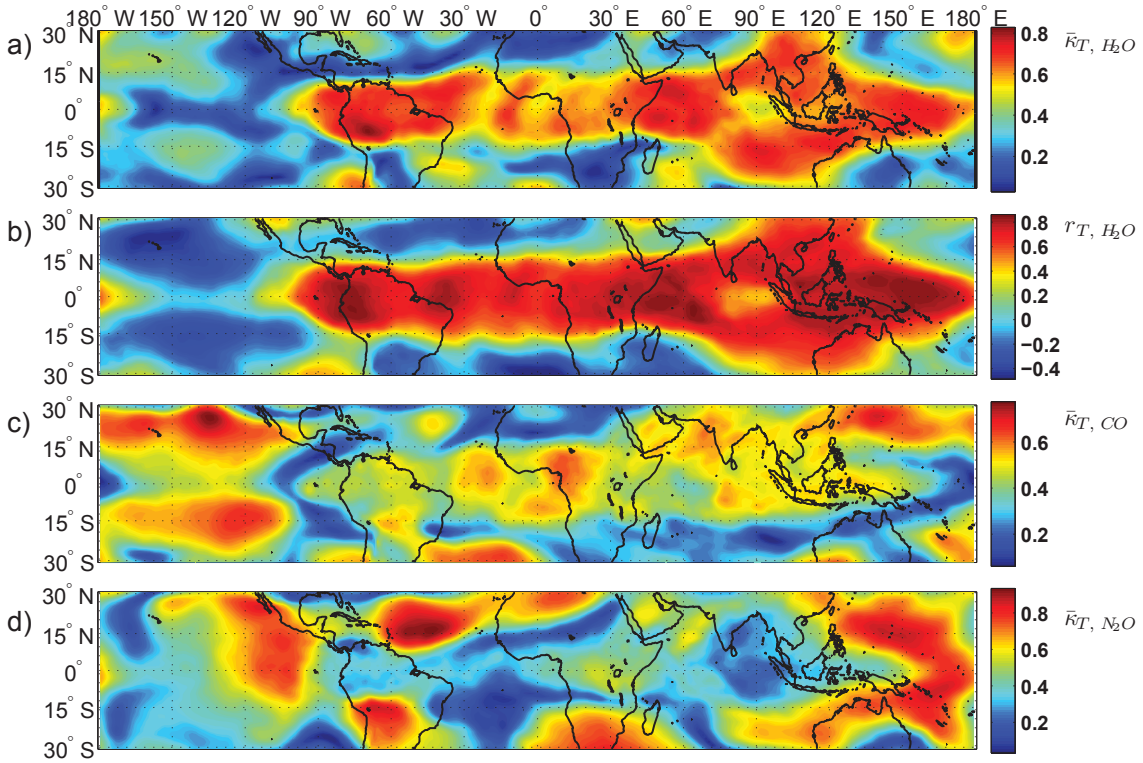

Figure 4.2: (a) $\bar{\kappa}_{T,H_2O}$, b) r_{T,H_2O} using 140 day lag, c) $\bar{\kappa}_{T,CO}$, d) $\bar{\kappa}_{T,N_2O}$.

The multiyear H_2O $\bar{\kappa}$ map given in Figure 4.2a shows that $\bar{\kappa}$ is enhanced at almost all longitudes within the 15^o S-15^o N latitude band except the eastern Pacific (90^o W-180^o W). Within this band, there are areas of larger $\bar{\kappa}$ over South America, the Indian Ocean, and the

maritime continent. Large $\bar{\kappa}$ at a particular grid point does not neccessarilly imply that air parcels advected through this grid point are dehydrated by cold anomalies at that location. At the 100 hPa level, monthly mean temperatures are strongly correlated across distances of several thousand kms (*Folkins*, 2012). Rather than being sites of active dehydration, some of the large values of $\bar{\kappa}$ on the 100 hPa surface can probably be attributed to a coherence with the temperature fluctuations of a region where dehydration does occur. Regions of highest final dehydration density have been identified using trajectory models (e.g., *Schoeberl and Dessler*, 2011). The dehydration regions fall within the enhanced $\bar{\kappa}$ regions shown in Figure 4.2a. There are also several regions of enhanced $\bar{\kappa}$ that are associated with very weak dehydration density, particularly the Indian Ocean. Regions where final dehydration occurs should exhibit enhanced $\bar{\kappa}$, but the reverse need not be true.

Figure 4.2c shows the multiyear CO $\bar{\kappa}$ map. The most prominent features of this map are the large regions of high $\bar{\kappa}$ in the subtropical Pacific on both sides of the equator. Figure 4.3 shows the $\bar{\kappa}$ maps associated with temperature anomalies on the 100 hPa surface, and the U50 and the global ENSO indices. The Pacific dipole pattern (*Randel et al.*, 2000; *Zhou et al.*, 2004; *Trenberth and Smith*, 2006) is a common feature of both maps. On multiyear timescales, CO anomalies in the lower stratosphere are coherent with temperature variability on the 100 hPa surface that is associated with the QBO and ENSO.

The Pacific dipole is usually associated with ENSO (*Randel et al.*, 2000; *Zhou et al.*, 2004; *Trenberth and Smith*, 2006) , whereas the QBO is associated with zonally symmetric temperature anomalies more strongly confined to the tropics (*Huesmann and Hitchman*, 2001; *Pascoe et al.*, 2005; *Liang et al.*, 2011). During the MLS observing period used here (2005 - 2010), the fact that the QBO and ENSO were mostly in phase (*Liang et al.*, 2011) could account for the similarity of the QBO and ENSO $\bar{\kappa}$ maps shown in Figure 4.3 .

Figure 4.2d shows the multiyear N_2O $\bar{\kappa}$ map. This pattern does not show a Pacific dipole, but does show a boomerang shaped structure in the West Pacific. This pattern is associated with enhanced convective heating along the equator (*Tian et al.*, 2006), and was previously seen in the RMM1 $\bar{\kappa}$ pattern.

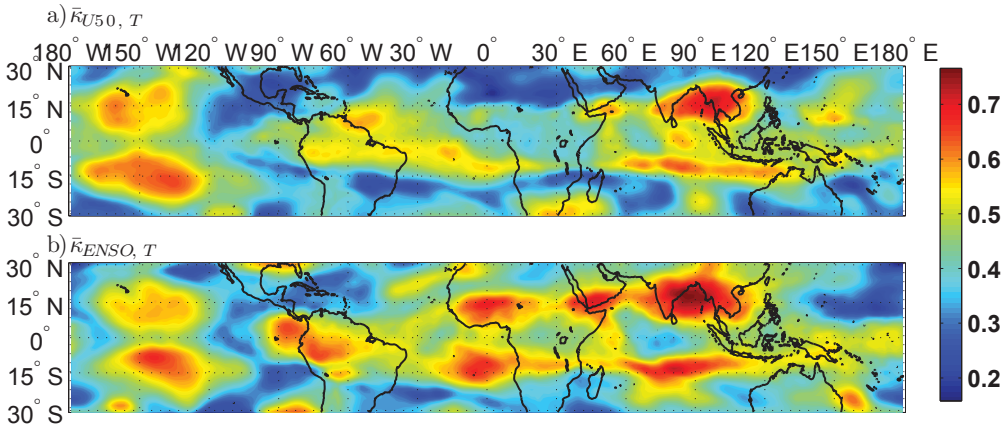

Figure 4.3: $\bar{\kappa}$ using 100 hPa T anomalies and (a) U50 and (b) global ENSO index.

4.3 H_2O Lagged Correlation Map

The relationship between temperature anomalies on the 100 hPa surface and the mixing ratios of chemical tracers in the lower stratosphere can also be studied using lagged correlation maps. The temperature and tracer anomalies are first band pass filtered using a particular time window. The correlation between the temperature anomaly time series at a particular grid point and the mean tracer mixing ratio is then calculated with a particular time lag. Figure 4.2b shows the lagged correlation map for H_2O using the multiyear time window and a 140 days time lag. This value of the time lag resulted in the largest average correlation over the 30^o S - 30^o N latitude range. The lagged correlation map is very similar to the $\bar{\kappa}$ map, but does exhibit a stronger dipole structure in the eastern Pacific than the multiyear H_2O $\bar{\kappa}$ map. Figure 4.3 shows that this feature is associated with both QBO and ENSO variability, during the 2005 - 2010 time period considered here. Cold temperature anomalies within the Pacific dipole pattern are associated, on the 100 hPa surface, with positive ENSO phase (i.e. El Nino) (*Weare*, 2008).

For CO and N_2O, the time lag which maximized the correlation was not well defined. Lagged correlation maps for these tracers are therefore not shown.

4.4 Weighted Mean Time Lags

At a given frequency ω, the time lag between the chemical tracer (here H_2O) and 100 hPa temperature anomalies is equal to the phase spectrum ($\Phi_{T,H_2O}(\omega)$) divided by frequency (ω).

$$\tau(\omega) = \frac{\Phi_{T,H_2O}(\omega)}{\omega} \tag{4.1}$$

Over a particular frequency window, $[\omega_1, \omega_2]$, we define the following effective coherence weighted mean time lag.

$$\bar{\tau} = \frac{\int_{\omega_1}^{\omega_2} \kappa^2_{T,H_2O}(\omega)(\frac{\Phi_{H_2O}(\omega)}{\omega})d\omega}{\int_{\omega_1}^{\omega_2} \kappa^2_{T,H_2O}(\omega)d\omega} \tag{4.2}$$

The above expression is used to calculate the mean time lags in the subseasonal and multiyear time windows. Figures 4.4a-c show subseasonal $\bar{\tau}$ vs $\bar{\kappa}$ scatterplots for the three tracers. The thick solid lines indicate the mean dependence of $\bar{\tau}$ on $\bar{\kappa}$. One would expect $\bar{\tau}$ to converge to a physically significant value for larger values of $\bar{\kappa}$. This is not the case for N_2O, where the mean value of $\bar{\tau}$ is near zero for all $\bar{\kappa}$. However, this is consistent with our previous finding of the lack of any physically significant relationship between the N_2O and 100 hPa temperature anomalies on subseasonal timescales. For CO, $\bar{\tau}$ converges to 5 days at large $\bar{\kappa}$. For H_2O, the mean time lag appears to decrease at large $\bar{\kappa}$. However, this decrease may be attributable to the lower number of grid cells with high $\bar{\kappa}$. For $\bar{\kappa}$ larger than 0.4, the mean time lags for H_2O and CO in the subseasonal time windows are 2.51 and 3.16 days respectively.

The subseasonal time lags of 2.51 and 3.16 days for H_2O and CO are much smaller than would be expected to occur in association with changes in stratospheric entry mixing ratio. Using an annual mean ascent rate of 0.25 mm s^{-1} (*Randel et al.*, 2008), the timescale for a change in stratospheric entry mixing ratio of a tracer to be advected by slow ascent to the center of the 68 hPa MLS kernel is roughly 100 days. On subseasonal timescales, the fluctuations in lower stratospheric H_2O and CO that are coherent with 100 hPa temperature can therefore be attributed to the effect of upwelling fluctuations on the local tendency for vertical advection.

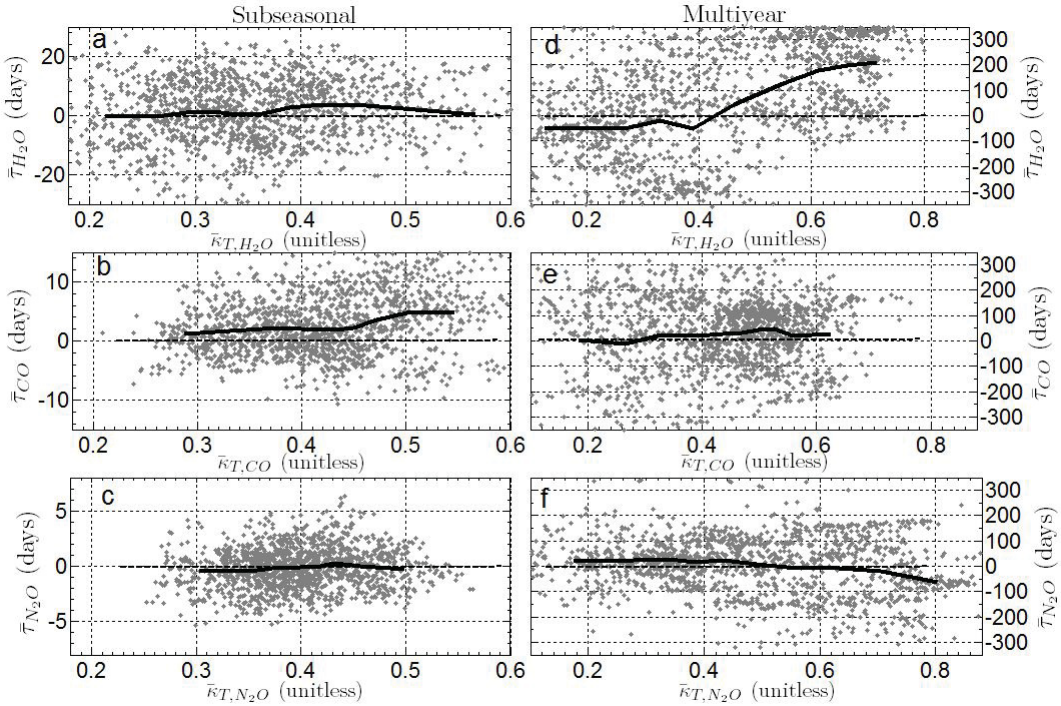

Figure 4.4: Scatter plots of the mean time lag $\bar{\tau}$ against $\bar{\kappa}$ for the subseasonal (a-c) and multiyear (d-f) time windows. The solid lines refer to the mean dependence of $\bar{\tau}$ on $\bar{\kappa}$.

Figure 4.4d shows that, on multiyear timescales, the mean value of the H_2O $\bar{\tau}$ converges to 200 days at high $\bar{\kappa}$. For $\bar{\kappa}$ larger than 0.4, the mean multiyear H_2O time lag is 140 days. This time lag is roughly equal to the time required for an air parcel to be advected by slow ascent the 2.2 km vertical distance from 100 hPa ($\sim$ 16.6 km) to the center of the 68 hPa ($\sim$ 18.8km) averaging kernel ($\sim$ 100 days). On multiyear timescales, the fluctuations in lower stratospheric water vapor that are coherent with 100 hPa temperature originate mainly from changes in the stratospheric entry mixing ratio.

For H_2O (and other ice soluble tracers), there is a direct physical mechanism which couples TTL temperature fluctuations to changes in the mean stratospheric entry mixing ratio (*Fueglistaler and Haynes*, 2005). Dry tracers such as CO and N_2O are not coupled to 100 hPa temperature fluctuations through the Clausius - Clapeyron relationship. However, there can be an indirect coupling mediated through changes in convective outflow. Cold anomalies in the TTL are ordinarilly coupled to increases in upwelling (*Randel et al.*, 2002). The primary mass source for this upwelling is outflow from deep convection. If the

upwelling mass flux increases, a higher fraction of deep convective outflow must ascend into the stratosphere. This can be accomplished either by an increase in the altitude of convective outflow, or by a decrease in the Level of Zero radiative Heating (LZH). Both of these changes appear to occur in response to increased upwelling during Northern Hemisphere winter (*Folkins et al.*, 2006). The relative effect of this mechanism on tracer mixing ratios should be largest at heights where the convectively induced changes in the tracer age spectrum (the elapsed time since convective detrainment) are comparable with the age of the tracer itself. This is most likely to occur in the TTL where high altitude outflow occurs, and less likely to occur in the lower stratosphere where air parcels are much older.

The solid line in Figure 4.4e shows the dependence of the mean multiyear CO $\bar{\tau}$ on $\bar{\kappa}$. There is a tendency toward positive $\bar{\tau}$ at larger $\bar{\kappa}$. The mean $\bar{\tau}$ for $\bar{\kappa}$ larger than 0.4 is 33 days. This time lag is significantly shorter than the timescale associated with upward transport from 100 hPa to 68 hPa ($\sim$ 100 days). It is therefore unlikely that the multiyear anomalies in lower stratospheric CO originate mainly from changes in stratospheric entry mixing ratio (e.g. from changes in convective outflow). However, the roughly tenfold increase in the time lag in going from subseasonal to multiyear timescales (3.16 days to 33 days) is roughly consistent with the increase in the subseasonal to multiyear time windows (from 40 - 107 days to 682 - 2048 days). The average phase offset between 100 hPa temperature and 68 hPa CO fluctuations in the subseasonal time window is therefore roughly equal to the average phase offset in the multiyear time window. This suggests that the multiyear 68 hPa CO fluctuations are also coupled to 100 hPa temperature fluctuations mainly through the effect of upwelling on the local tendency for vertical advection.

Figure 4.4f shows that the mean multiyear $\bar{\tau}$ for N_2O converges to roughly -50 days for large $\bar{\kappa}$. On multiyear timescales, N_2O anomalies in the lower stratosphere therefore precede 100 hPa temperature anomalies. The dynamical mechanism most likely to give rise to this kind of downward phase propagation is the QBO, which descends at rate of approximately 1 km per month (*Baldwin et al.*, 2001). This rate of descent would be consistent with a 65 day time lag for the 2.2 km descent from the center of the 68 hPa ($\sim$ 18.8 km) N_2O averaging kernel to the 100 hPa ($\sim$ 16.6 km) level. The similarity of these

timescales, and the prominence of the QBO related features in the $\bar{\kappa}$ map (for the 2005 - 2010 period), indicates that the multiyear variability of N_2O in the lower stratosphere is directly induced by the QBO. This is in contrast, for example, to the case of H_2O, where the QBO induced variability occurs indirectly through modulations in TTL temperature, which then subsequently affect the H_2O stratospheric entry mixing ratio (*Fueglistaler and Haynes*, 2005).

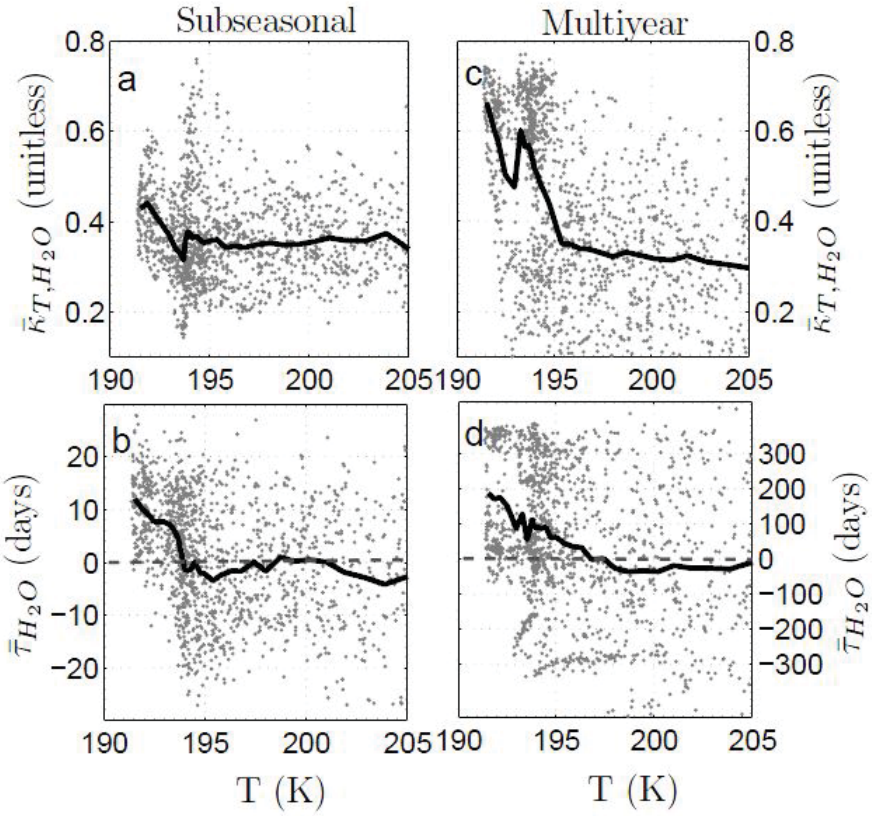

Figure 4.5: (a) Subseasonal $\bar{\kappa}$ against annual mean MERRA temperature for grid boxes on the 100 hPa surface; (b) subseasonal $\bar{\tau}$ against annual mean 100 hPa MERRA temperature. Plots (c) and (d) are the same as (a) and (b), except that $\bar{\kappa}$ and $\bar{\tau}$ refer to the multiyear time window. In each plot, the solid lines show the mean dependence of $\bar{\kappa}$, or $\bar{\tau}$, on temperature.

The time lag plots shown in Figures 4.5 demonstrate that, while the lower stratospheric water vapor fluctuations on subseasonal timescales are mainly generated by the effect of upwelling on the local tendency for vertical advection, water vapor fluctuations on multiyear timescales are mainly generated by fluctuations in the stratospheric entry mixing

ratio. Figures 4.5a, c show scatterplots of $\bar{\kappa}$ against annual mean temperature for each grid point on the 100 hPa surface. In the subseasonal time window, $\bar{\kappa}$ is almost independent of temperature. In the multiyear time window, there is a sharp increase in $\bar{\kappa}$ for temperatures colder than 194 K. These results are also consistent with the view that, although dehydration plays a minor role in lower stratospheric water vapor fluctuations on subseasonal timescales, TTL dehydration dominates lower stratospheric water variability on multiyear timescales.

In Figure 4.5b the subseasonal $\bar{\tau}$ for H_2O is plotted against annual mean temperature. The mean $\bar{\tau}$ is near zero for most values of temperature, but sharply increases to 10 days for temperatures less than 194 K. The origin of the increase in $\bar{\tau}$, despite the absence of an increase in $\bar{\kappa}$ is unclear. One possibility is that dehydration is playing a minor role in water vapor variability on subseasonal timescales. Because of the 100 days timescale for vertical advection from 100 hPa to the 68 pressure surface ($\sim$ 100 days), a small amount of TTL dehydration could generate a $\bar{\tau} \sim 10$ days at cold temperatures, while introducing only a small increase in $\bar{\kappa}$.

Figure 4.5d shows a scatterplot of the multiyear $\bar{\tau}$ for H_2O plotted against annual mean temperature. There is a gradual increase in $\bar{\tau}$ at colder temperatures, reaching a value close to 180 days for annual mean temperaures equal to 192 K. This increase is also consistent with an increasing role for dehydration at colder temperature.

CHAPTER 5

CONCLUSION

This thesis has examined the coherence in the tropics between temperature fluctuations on the 100 hPa surface and fluctuations in the lower stratospheric mixing ratios of H_2O, CO, and N_2O. Due to changes in the relative importance of different dynamical modes at different timescales, we have done separate calculations of the coherence in the subseasonal and multiyear time windows. On subseasonal timescales, the dominant features in the coherence pattern between fluctuations in 100 hPa temperature and water vapor are two Rossby lobes in the Indian Ocean extending symmetrically from both sides of the equator. The 68 hPa H_2O mixing ratio anomalies are almost synchronous with the anomalies in 100 hPa temperature. At larger values of coherence (the $\bar{\kappa}$ statistic), the 68 hPa water vapor anomalies lag fluctuations in 100 hPa temperature by 2.5 days. On subseasonal timescales, the variability of water vapor in the lower tropical stratosphere is therefore dominated by variability in upwelling associated with the dissipation of Rossby waves (i.e. the BLN mechanism). However, the increase in the time lag $\bar{\tau}$ at colder temperatures is consistent with a minor role for dehydration in the subseasonal time window.

The spatial pattern of the coherence between lower stratospheric water vapor and 100 hPa temperature anomalies on multiyear timescales has no resemblance to the coherence pattern on subseasonal time scales. Whereas the subseasonal coherence pattern is dominated by two Rossby lobes, and is associated with values of $\bar{\kappa}$ that are independent of temperature, the multiyear coherence pattern covers a much larger geographic area and is strongly shaped by the annual mean pattern in 100 hPa temperature. In particular, the mean value

of the multiyear $\bar{\kappa}$ increases sharply for annual mean temperatures colder than 194 K. In addition, the time lag between the multiyear anomalies in lower stratospheric water vapor and 100 hPa temperature increases with both colder temperature and higher $\bar{\kappa}$, approaching a maximum value of 200 days. This timescale is equal to the time required for the vertical ascent of an air parcel from the 100 hPa surface to the top of the 68 hPa MLS H_2O kernel. These results demonstrate that the multiyear variability in lower stratospheric water vapor is dominated by temperature fluctuations in the TTL which affect the water vapor stratospheric entry mixing ratio by modulating the amount of dehydration. It should be noted, however, that due to long distance correlations between temperature fluctuations on the 100 hPa surface, not all locations on the 100 hPa surface with large $\bar{\kappa}$ are likely to play a role in the dehydration of air parcels entering the stratosphere.

The rate of lower stratospheric upwelling from the BLN mechanism can be expected to be modulated by changes in both the intensity and location of tropical convection (*Ryu and Lee*, 2010). As the main source of variability of tropical convection in the subseasonal window, the MJO would therefore be expected to modulate the rate of lower stratospheric upwelling in this frequency range. We compared the spatial pattern of the coherence between the subseasonal anomalies in lower stratospheric CO and 100 hPa temperature to the spatial pattern of the coherence between the RMM1 MJO index and 100 hPa temperature. Both coherence patterns were evaluated over the January 1, 2005 - December 31, 2010 time interval. The two patterns were very similar, especially in the western tropical Pacific. In this region, both patterns exhibited a typical Gill type response with Rossby lobes spreading to the west and a Kelvin response spreading east toward the dateline. The MJO therefore plays a significant role in modulating the variability of lower stratospheric CO on subseasonal timescales. This finding is consistent with previous results showing that the MJO affects the distribution of ozone (*Weare*, 2010) and water vapor (*Mote et al.*, 1998) in the lower tropical stratosphere, and the variability of CO in the TTL (*Wong and Dessler*, 2007).

The map of the coherence between the multiyear lower stratospheric CO and 100 hPa anomalies exhibited a strong Pacific dipole. This feature is usually characteristic of ENSO (*Randel et al.*, 2000; *Zhou et al.*, 2004; *Trenberth and Smith*, 2006). However, during the

time period analyzed here, this pattern was coherent with both the QBO and ENSO, so that the relative roles of these multiyear dynamical modes could not be differentiated. However, for larger values of $\bar{\kappa}$, the phase difference between the CO and 100 hPa temperature anomalies in the multiyear time window was similar to the phase difference in subseasonal time window. This suggests that the main mechanism through which variability in lower stratospheric upwelling generated CO anomalies on multiyear timescales was also through modulations of the local tendency for vertical advection.

In global chemistry climate models, it is often difficult to know whether the mechanisms for Stratosphere - Troposphere Exchange (STE) and TTL dehydration are being accurately modelled. This is partly because many of the STE exchange mechanisms involve small scale convective or cloud scale processes that are parameterized rather than explicitly modelled, and also because of difficulties in making more general conclusions from a limited number of *in situ* measurements. However, the statistical methods used here could be applied to output from climate models. Accurate simulations of the coherence between 100 hPa temperature fluctuations and the anomalies in lower stratospheric tracers, in different time windows, would give greater credibility to the future trends in stratospheric chemical constituents predicted by these models (*Butchart et al.*, 2011). This type of analysis would be particularly important in the case of water vapor. The transport of condensable tracers like water vapor through the TTL is affected by a larger number of physical mechanisms than the transport of dry tracers, and calculations have suggested that past and future trends in stratospheric water vapor can exhibit a significant radiative forcing on climate (*Solomon et al.*, 2010).

BIBLIOGRAPHY

Anthes, R. A., C. Rocken, and Y. H. Kuo, Applications of COSMIC to meteorology and climate, *Terr. Atmos. Oceanic Sci.*, *11*, 115–156, 2000.

Anthes, R. A., et al., The COSMIC/FORMOSAT-3 mission: Early results, *B. Am. Meteorol. Soc.*, *89*, 313–333, 2008.

Baldwin, M. P., et al., The quasi-biennial oscillation, *Rev. Geophys.*, *39*, 179–229, 2001.

Bernath, P. F., et al., Atmospheric Chemistry Experiment (ACE): Mission overview, *Geophys. Res. Lett.*, *32*, L15S01, 2005.

Bjerknes, J., Atmospheric teleconnections from the equatorial Pacific, *Mon. Wea. Rev.*, *97*, 163–172, 1969.

Boehm, M. T., and S. Lee, The implications of tropical Rossby waves for tropical tropopause cirrus formation and for the equatorial upwelling of the Brewer-Dobson circulation, *J. Atmos. Sci.*, *60*, 247–261, 2003.

Bosilovich, M. G., J. Chen, F. R. Robertson, and R. F. Adler, Evaluation of global precipitation in reanalyses, *J. Appl. Meteor. Climatol.*, *47*, 2279–2299, 2008.

Bouttier, F., and F. Rabier, The operational implementation of 4D-Var, *ECMWF Newsletter*, pp. 2–5, 1997.

Butchart, N., et al., Multimodel climate and variability of the stratosphere, *J. Geophys. Res.*, *116*, D05102, 2011.

Calvo, N., R. R. Garcia, and W. J. R. D. R. Marsh, Dynamical mechanism for the increase in tropical upwelling in the lowermost tropical stratosphere during warm ENSO events, *J. Atmos. Sci.*, *67*, 2331–2340, 2010.

Crutzen, P. J., Nobel Lecture: My Life with O_3, NO_x and Other YZOxs, *Nobelprize.org.*, p. July11 2012, 1995.

Crutzen, P. J., and P. H. Zimmermann, The changing photochemistry of the troposphere, *Tellus*, *43AB*, 136–151, 1991.

D'Amelio, M. T. S., L. V. Gatti, J. B. Miller, and P. Tans, Regional N_2O fluxes in Amazonia derived from aircraft vertical profiles, *Atmos. Chem. Phys.*, *9*, 8785–8797, 2009.

Dee, D. P., and S. Uppala, Variational bias correction of satellite radiance data in the ERA-Interim reanalysis, *Q. J. R. Meteorol. Soc., in press*, *135*, 1830–1841, 2009.

Dessler, A. E., A reexamination of the stratospheric fountain hypothesis, *Geophys. Res. Lett.*, *25*, 4165–4168, 1998.

Dessler, A. E., The effect of deep, tropical convection on the tropical tropopause layer, *J. Geophys. Res.*, *4033*, 2002.

Dessler, A. E., and S. C. Sherwood, A model of HDO in the tropical tropopause layer, *Atmos. Chem. Phys.*, *3*, 4489–4501, 2003.

Duchon, C. E., Lanczos filtering in one and two dimensions, *J. Appl. Meteor.*, *18*, 1016–1022, 1979.

Dunkerton, T. J., A two- Demensional model of the Quasi-Biennial Oscillation, *J. Atmos. Sci.*, *42*, 1151–1160, 1985.

Dunkerton, T. J., Quasi- biennial and subbiennial variations of stratospheric trace constituents derived from HALOE observations, *J. Atmos. Sci.*, *58*, 7–25, 2001.

Folkins, I., Height increase of the melting level stability anomaly in the tropics, *Atmos. Chem. Phys. Discuss.*, *12*, 11567–11594, 2012.

Folkins, I., M. Loewenstein, J. Podolske, S. J. Oltmans, and M. Proffitt, A barrier to vertical mixing at 14 km in the tropics: Evidence from ozonesondes and aircraft measurements, *J. Geophys. Res.*, *104*, 22095–22102, 1999.

Folkins, I., P. Bernath, C. Boone, G. Lesins, N. Livesey, A. M. Thompson, K. Walker, and J. C. Witte, Seasonal cycles of O_3, CO, and convective outflow at the tropical tropopause, *Geophys. Res. Lett.*, *33*, L16802, 2006.

Forster, P., et al., Changes in atmospheric constituents and in radiative forcing. in: Climate change 2007: The physical science basis. Contribution of working group I to the fourth assessment report of the Intergovernmental Panel on Climate Change., *Cambridge University Press , Cambridge, United Kingdom and New York, NY, USA*, 2007.

Forster, P. M. D., and K. P. Shine, Stratospheric water vapour changes as a possible contributor to observed stratospheric cooling, *Geophys. Res. Lett.*, *26*, 3309–3312, 1999.

Fueglistaler, S., and P. H. Haynes, Control of interannual and longer-term variability of stratospheric water vapor, *J. Geophys. Res.*, *110*, D24108, 2005.

Fueglistaler, S., H. Wernli, and T. Peter, Tropical troposphere-to-stratosphere transport inferred from trajectory calculations, *J. Geophys. Res.*, *109*, D03108, 2004.

Fueglistaler, S., A. E. Dessler, T. J. Dunkerton, I. Folkins, Q. Fu, and P. W. Mote, Tropical tropopause layer, *Rev. Geophys.*, *4,*, RG1004, 2009.

Garcia, R., and M. Salby, Transient response to localized episodic heating in the tropics. part II: Far-field behavior, *J. Atmos. Sci.*, *44*, 499–530, 1987.

Garcia, R. R., and W. J. Randel, Acceleration of the Brewer Dobson circulation due to increases in greenhouse gases, *J. Atmos. Sci.*, *65*, 2731–2739, 2008.

Garny, H., M. Dameris, W. Randel, G. E. Bodeker, and R. Deckert, Dynamically forced increase of tropical upwelling in the lower stratosphere, *J. Atmos. Sci.*, *68*, 1214–1233, 2011b.

Gettelman, A., and P. M. de F. Forster, A climatology of the tropical tropopause layer, *Journal of the Meteorological Society of Japan*, *80*, 911–924, 2002.

Gettelman, A., J. R. Holton, and A. R. Douglass, Simulations of water vapor in the lower stratosphere and upper troposphere, *J. Geophys. Res.*, *105*, 9003–9023, 2000.

Gettelman, A., W. J. Randel, S. Massie, F. Wu, W. G. Read, and J. M. Russell, El Nino as a natural experiment for studying the tropical tropopause region, *J. Climate.*, *14*, 3375–3392, 2001.

Gettelman, A., M. L. Salby, , and F. Sassi, Distribution and influence of convection in the tropical tropopause region, *J. Geophys. Res.*, *107*, 40–80, 2002.

Gill, A., Some simple solutions for heat-induced tropical circulations, *Quart. J. Roy. Meteor. Soc.*, *106*, 447–462, 1980.

Hans, V. S., and W. Z. Francis, *Statistical analysis in climate research*, virtual ed., Cambridge University Press (Virtual Publishing), 2003.

Haynes, P., Stratospheric dynamics, *Ann. Rev. Fluid Mech.*, *37*, 263–293, 2005.

Hegglin, M. I., and T. G. Shepherd, Large climate-induced changes in ultraviolet index and stratosphere-to-troposphere ozone flux, *Nature Geoscience*, *2*, 687–691, 2009.

Hendon, H. H., and M. L. Salby, The life cycle of the Madden-Julian oscillation, *J. Atmos. Sci.*, *51*, 2225–2237, 1994.

Holton, J. R., and A. Gettelman, Horizontal transport and the dehydration of the stratosphere, *Geophys. Res. Lett.*, *28*, 2799–2802, 2001.

Holton, J. R., and R. S. Lindzen, An updated theory for the Quasi-Biennial Cycle of the tropical stratosphere, *J. Atmos. Sci.*, *29*, 107–1080, 1972.

Holton, J. R., P. H. Haynes., M. E. McIntyre., A. R. Douglass., R. B. Rood., and L. Pfister, Stratosphere-troposphere exchange, *Rev. Geophys.*, *33*, 403–439, 1995.

Huesmann, A. S., and M. H. Hitchman, The stratospheric quasibiennial oscillation in the NCEP reanalyses: Climatological structures, *J. Geophys. Res.*, *106*, 11,859–11,874., 2001.

Jacob, D. J., *Introduction to Atmospheric Chemistry*, Princeton University Press, New Jersy, 1999.

Jiang, N., J. D. Neelin, and M. Ghil, Quasi-quadrennial and quasi-biennial variability in COADS equatorial Pacific sea surface temperature and winds, *Clim. Dyn.*, *12*, 101–112, 1995.

Jin, F.-F., and B. J. Hoskins, The direct response to tropical heating in a baroclinic atmosphere., *J. Atmos. Sci.,*, *52*, 307–319, 1995.

Kalnay, E., et al., The NCEP/NCAR 40-year reanalysis project, *B. Am. Meteorol. Soc.*, *77*, 437–471, 1996.

Kerr-Munslow, A. M., and W. A. Norton, Tropical wave driving of the annual cycle in tropical tropopause temperatures. Part I: ECMWF analyses, *J. Atmos. Sci.*, *63*, 1410–1419, 2006.

Lambert, A., et al., Validation of the Aura Microwave Limb Sounder middle atmosphere water vapor and nitrous oxide measurements, *J. Geophys. Res.*, *112*, D24S36, 2007.

Liang, C. K., A. Eldering, A. Gettelman, B. Tian, S. Wong, E. J. Fetzer, and K. N. Liou, Record of tropical interannual variability of temperature and water vapor from a combined AIRS-MLS data set, *J. Geophys. Res.*, *116*, D06103, 2011.

MacMynowski, D. G., and E. Tziperman, Factors affecting ENSO's period, *J. Atmos. Sci.*, *65*, 1570–1586, 2008.

Madden, R., and P. Julian, Description of global-scale circulation cells in the tropics with a 40-50 day period, *J. Atmos. Sci.*, *29*, 1109–1123, 1972.

Madden, R. A., and P. Julian, Detection of a 40-50 day oscillation in the zonal wind in the Tropical Pacific, *J. Atmos. Sci.*, *28*, 702–708, 1971.

Majda, A. J., and S. N. Stechmann, Nonlinear dynamics and regional variations in the MJO skeleton, *J. Atmos. Sci.*, *68*, 3053–3071, 2011.

Martius, O., C. Schwierz, and M. Sprenger, Dynamical tropopause variability and potential vorticity streamers in the northern hemisphere - A climatological analysis, *Advances in atmospheric sciences*, *25*, 367–379, 2008.

McLean, J. D., C. R. de Freitas, and R. M. Carter, Influence of the Southern Oscillation on tropospheric temperature, *J. Geophys. Res.*, *114*, D14104, 2009.

Monier, E., B. C. Weare, and W. I. Gustafson, The Madden-Julian oscillation wind-convection coupling and the role of moisture processes in the MM5 model, *Clim. Dyn.*, *35*, 435–447, 2010.

Mote, P. W., T. J. Dunkerton, and H. C. Pumphrey, Subseasonal variations in lower stratospheric water vapor, *Geophys.Res. Lett.*, *25*, 2445–2448, 1998.

Mote, P. W., et al., An atmospheric tape recorder: The imprint of tropical tropopause temperatures on stratospheric water vapor, *J. Geophys. Res.*, *101*, 3989–4006, 1996.

Naujokat, B., An update of the observed quasi-biennial oscillation of the stratospheric winds over the tropics, *J. Atmos. Sci.*, *43*, 1873–1877, 1986.

Neelin, J. D., D. S. Battisti, A. C. Hirst, F.-F. Jin, Y. Wakata, T. Yamagata, and S. E. Zebiak, ENSO theory, *J. Geophys. Res.*, *103*, 14,261–14,290, 1998.

Newell, R. E., and S. Gould-Stewart, A stratospheric fountain?, *J. Atmos. Sci.*, *38*, 2789–2796, 1981.

Nishimoto, E., and M. Shiotani, Seasonal and interannual variability in the temperature structure around the tropical tropopause and its relationship with convective activities, *J. Geophys. Res*, *117*, D02104, 2012.

Norton, W. A., Tropical wave driving of the annual cycle in tropical tropopause temperatures. Part II: Model results, *J. Atmos. Sci.*, *63*, 1420–1431, 2006.

Okumura, Y. M., and C. Deser, Asymmetry in the duration of El Ninõ and La Ninã, *J. Climate.*, *23*, 5826–5843, 2010.

Oliver, E. C. J., and K. R. Thompson, Madden-Julian Oscillation and sea level: Local and remote forcing, *J. Geophys. Res.*, *115*, C01003, 2010.

Oltmans, S. J., H. V omel, D. J. Hofmann, K. H. Rosenlof, and D. Kley, The increase in stratospheric water vapor from balloonborne, frostpoint hygrometer measurements at washington, D.C., and Boulder, Colorado, *Geophys. Res. Lett.*, *27*, 3453–3456, 2000.

Pascoe, C. L., L. J. Gray, S. A. Crooks, M. N. Juckes, and M. P. Baldwin, The quasi-biennial oscillation: Analysis using ERA-40 data, *J. Geophys. Res.*, *110*, D08105, 2005.

Plumb, R. A., A tropical pipe model of stratospheric transport, *J. Geophys. Res.*, *101*, 3957–3972, 1996.

Priestley, M. B., *Spectral analysis and time series*, Probability and mathematical statistics, London : Academic Press, 1981.

Pumphrey, H. C., C. Boone, K. A. Walker, P. Bernath, and N. J. Livesey, Tropical tape recorder observed in HCN, *Geophys. Res. Lett.*, *35*, L05801, 2008.

Randel, W., F. Wu, and D. Gaffen, Interannual variability of the tropical tropopause derived from radiosonde data and NCEP reanalyses, *J. Geophys. Res.*, *105*, 15,509–15,523, 2000.

Randel, W., F. Wu, S. Oltmans, K. Rosenlof, and G. Nedoluha, Interannual changes of stratospheric water vapor and correlations with tropical tropopause temperatures, *J. Atmos. Sci.*, *61*, 2133–2148, 2004.

Randel, W. J., F. Wu, A. Gettelman, J. M. R. III, J. M. Zawodny, and S. J. Oltmans, Seasonal variation of water vapor in the lower stratosphere observed in Halogen Occultation Experiment data, *J. Geophys. Res.*, *106*, 14,313–14,325, 2001.

Randel, W. J., R. R. Garcia, and F. Wu, Time-dependent upwelling in the tropical lower stratosphere estimated from the zonal-mean momentum budget, *J. Atmos. Sci.*, *59*, 2141–2152, 2002.

Randel, W. J., R. Garcia, and F. Wu, Dynamical balances and tropical stratospheric upwelling, *J. Atmos. Sci.*, *65*, 3584–3595, 2008.

Randel, W. J., R. R. Garcia, N. Calvo, and D. Marsh, Enso influence on zonal mean temperature and ozone in the tropical lower stratosphere, *J. Geophys. Res.*, *36*, L15822, 2009.

Read, W. G., et al., Aura Microwave Limb Sounder upper tropospheric and lower stratospheric h_2o and relative humidity with respect to ice validation, *J. Geophys. Res.*, *112*, D24S35, 2007.

Rienecker, M., et al., The GEOS-5 Data Assimilation System-Documentation of versions 5.0.1 and 5.1.0, and 5.2.0. NASA Tech. Rep. Series on global modeling and data assimilation, *NASA/TM*, *27*, 2008.

Rienecker, M. M., et al., Merra: NASA Modern-Era Retrospective Analysis for Research and Applications, *J. Climate*, *24*, 3624–3648, 2011.

Rosenlof, K. H., Seasonal cycle of the residual mean meridional circulation in the stratosphere, *J. Geophys. Res.*, *100*, 5173–5191, 1995.

Rui, H., and B. Wang, Development characteristics and dynamic structure of tropical intraseasonal convection anomalies, *J. Atmos. Sci.*, *47*, 357–379, 1990.

Ryu, J.-H., and S. Lee, Effect of tropical waves on the Tropical Tropopause Transition Layer upwelling, *J. Atmos. Sci.*, *67*, 3130–3148, 2010.

Ryu, J.-H., S. Lee, and S.-W. Son, Vertically propagating kelvin waves and tropical tropopause variability, *J. Atmos. Sci.*, *65*, 1817–1837, 2008.

Schoeberl, M., and A. Dessler, Dehydration of the stratosphere, *Atmos. Chem. Phys.*, *11*, 8433–8446, 2011.

Schoeberl, M. R., B. N. Duncan, A. R. Douglass, J. Waters, N. Livesey, W. Read, and M. Filipiak, The carbon monoxide tape recorder, *J. Geophys. Res.*, *33*, L12811, 2008a.

Schoeberl, M. R., et al., QBO and annual cycle variations in tropical lower stratosphere trace gases from HALOE and Aura MLS observations, *J. Geophys. Res.*, *113*, D05301, 2008b.

Seidel, D. J., R. J. Ross, J. K. Angell, and G. C. Reid, Climatological characteristics of the tropical tropopause as revealed by radiosondes, *J. Geophys. Res.*, *06*, 7857–7878, 2001.

Seinfeld, J. H., and S. N. Pandis, *Atmospheric Chemistry and Physics: From Air Pollution to Climate Change*, Wiley-Interscience, New York, 1997.

Selkirk, H. B., The tropopause cold trap in the Australian monsoon during STEP/AMEX 1987, *J. Geophys. Res.*, *98*, 8591–8610, 1993.

Sherwood, S. C., A stratospheric drain over the maritime continent, *J. Geophys. Res.*, *27*, 677–680, 2000.

Solomon, S., K. H. Rosenlof, R. W. Portmann, J. S. Daniel, S. M. Davis, T. J. Sanford, and G.-K. Plattner, Contributions of stratospheric water vapor to decadal changes in the rate of global warming, *Science*, *327*, 1219–1223, 2010.

Steinwagner, J., S. Fueglistaler, G. Stiller, T. von. Clarmann, M. Kiefer, and P.-P. B. A. van Delden Thomas Röckmann, Tropical dehydration processes constrained by the seasonality of stratospheric deuterated water, *Nature Geosc.*, *3*, 262–266, 2010.

Tian, B., D. E. Waliser, E. J. Fetzer, B. H. Lambrigtsen, Y. L. Yung, and B. Wang, Vertical moist thermodynamic structure and spatial-temporal evolution of the MJO in AIRS observations, *J. Atmos. Sci.*, *63*, 2462–2485, 2006.

Tian, W. S., M. P. Chipperfield, and D. R. Lu, Impact of increasing stratospheric water vapor on ozone depletion and temperature change, *Adv. Atmos. Sci.*, *26*, 423–437, 2009.

Ting, M., and L. Yu, Steady response to tropical heating in wavy linear and nonlinear baroclinic models, *J. Atmos. Sci.*, *55*, 2565–2582, 1998.

Trenberth, K. E., and L. Smith, The vertical structure of temperature in the tropics: Different flavors of El Niño, *J. Climate*, *19*, 4956–4973, 2006.

Vömel, H., et al., Validation of Aura MLS water vapor by balloon borne cryogenic frostpoint hygrometer measurements, *J. Geophys. Res*, *112*, D24S37, 2007b.

Waters, J. W., et al., The Earth Observing System Microwave Limb Sounder (EOS MLS) on the Aura Satellite, *Geosci. Remote Sens.*, *44*, 1075–1092, 2006.

Waugh, D. W. L. O., S. R. Kawa, R. S. Stolarski, S. Pawson, A. R. Douglass, P. A. Newman, and J. E. Nielsen, Impacts of climate change on stratospheric ozone recovery, *Geophys. Res. Lett.*, *36*, L03805, 2009.

Weare, B. C., Multilag Singular Value Decomposition analysis of ENSO convection with tropical stratospheric temperature, *J. Climate*, *21*, 6556–6568, 2008.

Weare, B. C., Madden-Julian Oscillation in the tropical stratosphere, *J. Geophys. Res.*, *115*, D17113, 2010.

Wheeler, M. C., and H. H. Hendon, An all-season real-time multivariate MJO index: Development of an index for monitoring and prediction, *Mon. Wea. Rev.*, *132*, 1917–1932, 2004.

Wong, S., and A. E. Dessler, Regulation of H_2O and CO in tropical tropopause layer by the Madden-Julian oscillation, *J. Geophys. Res.*, *112*, D14305, 2007.

Zhang, C., Madden-Julian Oscillation, *Rev. Geophys.*, *43*, RG2003, 2005.

Zhou, X. L., M. A. Geller, and M. H. Zhang, Tropical Cold Point Tropopause characteristics derived from ECMWF reanalyses and soundings, *J. Climate*, *14*, 1823–1838, 2001.

Zhou, X. L., M. A. Geller, and M. Zhang, Temperature fields in the tropical tropopause transition layer, *J. Climate*, *17*, 2901–2908, 2004.